ELLIPSOIDAL AND HYPERBOLIC RADON TRANSFORMS; MICROLOCAL PROPERTIES AND INJECTIVITY

JAMES W. WEBBER[†], SEAN HOLMAN[‡], AND ERIC TODD QUINTO*

ABSTRACT. We present novel microlocal and injectivity analyses of ellipsoid and hyperboloid Radon transforms. We introduce a new Radon transform, R, which defines the integrals of a compactly supported L^2 function, f, over ellipsoids and hyperboloids with centers on a smooth connected surface, S. Our transform is shown to be a Fourier Integral Operator (FIO) and in our main theorem we prove that R satisfies the Bolker condition if the support of f is contained in a connected open set that is not intersected by any plane tangent to S. Under certain conditions, this is an equivalence. We give examples where our theory can be applied. Focusing specifically on a cylindrical geometry of interest in Ultrasound Reflection Tomography (URT), we prove injectivity results and investigate the visible singularities. In addition, we present example reconstructions of image phantoms in two-dimensions and validate our microlocal theory.

1. INTRODUCTION

In this paper, we introduce a novel Radon transform, R, which defines the integrals of compactly supported L^2 functions in $\mathbb{R}^n$ over ellipsoid, two-sheeted hyperboloid, and elliptic hyperboloid surfaces, with centers on a smooth, $(n-1)$-dimensional hypersurface, which we denote by S. R has applications in many imaging fields, such as Ultrasound Reflection Tomography (URT), Photoacoustic Tomography (PAT), ground penetrating radar, and Synthetic Aperture Radar (SAR). We present a novel microlocal and injectivity analysis of R, and determine the singularities (image edges) detected by R in examples of interest in URT.

The literature considers microlocal and injectivity analysis of spherical and ellipsoidal Radon transforms [14, 23, 34, 5, 32, 6, 2, 18, 26, 7, 17, 31, 24, 15, 25, 4]. Analytic uniqueness is considered in [18]. In [26], the authors consider a Radon transform, $\mathcal{R}$, which defines the integrals of an n-dimensional function over $(n-1)$-dimensional spheres with centers on a smooth, strongly convex hypersurface, denoted by $\mathcal{S}$ (using the notation of [26]). The authors show that $\mathcal{R}$ is a Fourier Integral Operator (FIO) with left projection that drops rank on planes tangent to $\mathcal{S}$. More precisely, the left and right projections of $\mathcal{R}$ are shown

to be Whitney folds. This means that there are artifacts in filtered backprojection type reconstructions from $\mathcal{R}f$ data which are reflections in hyperplanes tangent to $\mathcal{S}$.

In [2], the authors present a microlocal analysis of an elliptic Radon transform, $\mathcal{R}$ (to adopt the notation of [2]), of interest in two-dimensional URT. The authors consider a scanning modality, whereby a single emitter-receiver pair, kept a fixed distance apart, are rotated about the origin on lines tangent to the unit circle. The reflectivity function, which is the reconstruction target in URT, is supported on the interior of the unit circle. $\mathcal{R}f$ has two degrees of freedom, which are the major diameter of the ellipse, and the position of ellipse center, which lies on the unit circle and follows the emitter-receiver rotation. The authors prove that $\mathcal{R}$ is an elliptic FIO with conical relation, $\mathcal{C}$, which satisfies the Bolker condition. After which, it is shown that the normal operator of $\mathcal{R}$ is an elliptic Pseudodifferential Operator (PDO), order -1, and thus the inverse of $\mathcal{R}$ is stable on Sobolev scale $\frac{1}{2}$.

In [17], the authors consider a spherical Radon transform. The spheres of integration have centers restricted to cylindrical hypersurfaces of the form $\Gamma \times \mathbb{R}^m$, where Γ is a hypersurface in $\mathbb{R}^n$. The authors present a general methodology for inverting spherical Radon transforms with center set $\Gamma \times \mathbb{R}^m$. Specifically, the authors show that if an inversion formula is known for the center set Γ, then this can be extended to $\Gamma \times \mathbb{R}^m$. They apply the theory of [4], which provides inversion formulae for the spherical Radon transform with a flat plane center set, to derive inversion formulae for elliptic and circular cylinder center sets. Numerical results are also provided when the set of sphere centers is an elliptic cylinder, and the authors present simulated reconstructions of image phantoms from spherical integral data using the proposed formulae. A blurring effect is observed near sharp discontinuities in the image reconstructions, indicating that all singularities are not well resolved when the center set is an elliptic cylinder.

In our work, we introduce a novel Radon transform, denoted by R, which defines the integrals over ellipsoids and hyperboloids with centers on a smooth, connected surface, S. We show that R is an FIO. Our central theorem proves that R satisfies the Bolker condition if and only if $\text{supp}(f)$ is not intersected by any hyperplane tangent to S. The Bolker condition is important as it relates to image artifacts in filtered backprojection type reconstructions from Radon transform data, specifically to artifacts which are additional (unwanted) singularities in the reconstruction that are not in the object. Such artifacts are also often observed using iterative solvers and algebraic reconstruction techniques [37]. If the Bolker condition is satisfied, this implies reconstruction stability, and unwanted microlocal singularities are eliminated. Conversely, if the Bolker condition fails, the capacity for artifacts is amplified.

The calculations which determine satisfaction of Bolker shed light on the nature of the image artifacts (should they exist) if Bolker fails and can be used to predict artifact location and to help suppress artifacts [11, 36].

In a similar vein to [26], the left projection of R is shown to drop rank on planes which are tangent to S and we discover "mirror point" type artifacts which occur on opposite sides of planes tangent to S. Specifically, if the tangent planes to S do not intersect $\text{supp}(f)$, then we show that the artifacts are constrained to lie outside of $\text{supp}(f)$, and thus the Bolker condition holds. This is one of the central ideas of our main theorem. In [26], the surfaces of integration are spheres, which are symmetric about any plane through their center. This causes the reflection artifacts discovered in [26]. However, ellipsoids and hyperboloids do not share such symmetries, and thus the artifacts we discover are not reflections through planes

tangent to S, as in [26], but can be understood as a "perturbed" or "distorted" reflection. See Section 3.1, for a more detailed discussion on mirror point artifacts. The microlocal theory we present here is a generalization of the work of [26], to ellipsoid and hyperboloid integration surfaces.

After establishing our central microlocal theorems, we present a number of examples where our theory can be applied, some of which are relevant to URT. We focus on a cylindrical scanning geometry in $\mathbb{R}^3$, of interest in URT, and prove injectivity results. Specifically, we prove that any L^2 function, f, compactly supported on the interior of a unit cylinder in $\mathbb{R}^3$, can be reconstructed uniquely from its integrals over spheroids with centers on the unit cylinder. A unit cylinder in $\mathbb{R}^3$ is a special case of the more general cylindrical hypersurfaces considered in [17]. The authors of [17] consider spherical integral surfaces, whereas we consider, more general, spheroid integral surfaces. Our injectivity results hold for compactly supported L^2 functions, which advances the theory of [17], as their inversion formulae apply only to smooth functions of compact support. In addition, we show, using Volterra integral equation theory [30], that, with limited spheroid radii, one can reconstruct f on cylindrical tubes (or "layers") which are subsets of the unit cylinder interior. Limited sphere radii are not considered in [17]. We aim to address limited spheroid and sphere radii in this work.

The remainder of this paper is organized as follows. In section 2, we give some definitions from microlocal analysis that will be used in our theorems. In section 3, we define our generalized Radon transform and prove our main microlocal theorems, and follow up with some examples in section 3.2. In section 4, we investigate a cylindrical scanning geometry with applications in URT, and prove our main injectivity theorems. We also discuss in detail the visible singularities and show how the wavefront coverage varies with emitter/receiver discretization. To finish, in section 5, we present some example image reconstructions in two-dimensions and verify our microlocal theory.

2. Definitions from microlocal analysis

We next provide some notation and definitions. Let X and Y be open subsets of $\mathbb{R}^{n_X}$ and $\mathbb{R}^{n_Y}$, respectively. Let $\mathcal{D}(X)$ be the space of smooth functions compactly supported on X with the standard topology and let $\mathcal{D}'(X)$ denote its dual space, the vector space of distributions on X. Let $\mathcal{E}(X)$ be the space of all smooth functions on X with the standard topology and let $\mathcal{E}'(X)$ denote its dual space, the vector space of distributions with compact support contained in X. Finally, let $\mathcal{S}(\mathbb{R}^n)$ be the space of Schwartz functions, that are rapidly decreasing at ∞ along with all derivatives. See [33] for more information.

For a function f in the Schwartz space $\mathcal{S}(\mathbb{R}^{n_X})$ or in $L^2(\mathbb{R}^n)$, we use $\mathcal{F}f$ and $\mathcal{F}^{-1}f$ to denote the Fourier transform and inverse Fourier transform of f, respectively (see [19, Definition 7.1.1]). Note that $\mathcal{F}^{-1}\mathcal{F}f(\mathbf{x}) = \frac{1}{(2\pi)^{n_X}} \int_{\mathbf{y} \in \mathbb{R}^{n_X}} \int_{\mathbf{z} \in \mathbb{R}^{n_X}} \exp((\mathbf{x} - \mathbf{z}) \cdot \mathbf{y}) f(\mathbf{z}) \, \mathrm{d}\mathbf{z} \, \mathrm{d}\mathbf{y}$.

We use the standard multi-index notation: if $\alpha = (\alpha_1, \alpha_2, \ldots, \alpha_n) \in \{0, 1, 2, \ldots\}^{n_X}$ is a multi-index and f is a function on $\mathbb{R}^{n_X}$, then

$$\partial^\alpha f = \left(\frac{\partial}{\partial x_1}\right)^{\alpha_1} \left(\frac{\partial}{\partial x_2}\right)^{\alpha_2} \cdots \left(\frac{\partial}{\partial x_{n_X}}\right)^{\alpha_{n_X}} f.$$

If f is a function of $(\mathbf{y}, \mathbf{x}, \mathbf{s})$ then $\partial_{\mathbf{y}}^\alpha f$ and $\partial_{\mathbf{s}}^\alpha f$ are defined similarly.

We identify cotangent spaces on Euclidean spaces with the underlying Euclidean spaces, so we identify $T^*(X)$ with $X \times \mathbb{R}^{n_X}$. If Φ is a function of $(\mathbf{y}, \mathbf{x}, \mathbf{s}) \in Y \times X \times \mathbb{R}^N$ then we

define $d_{\mathbf{y}}\Phi = \left(\frac{\partial\Phi}{\partial y_1}, \frac{\partial\Phi}{\partial y_2}, \cdots, \frac{\partial\Phi}{\partial y_{n_X}}\right)$, and $d_{\mathbf{x}}\Phi$ and $d_{\mathbf{s}}\Phi$ are defined similarly. Identifying the cotangent space with the Euclidean space as mentioned above, we let $d\Phi = (d_{\mathbf{y}}\Phi, d_{\mathbf{x}}\Phi, d_{\mathbf{s}}\Phi)$. We use the convenient notation that if $\Omega \subset \mathbb{R}^m$, then $\dot{\Omega} = \Omega \setminus \mathbf{0}$.

The singularities of a function and the directions in which they occur are described by the wavefront set [9, page 16]:

Definition 2.1. Let X be an open subset of $\mathbb{R}^n$ and let f be a distribution in $\mathcal{D}'(X)$. Let $(\mathbf{x}_0, \boldsymbol{\xi}_0) \in X \times \dot{\mathbb{R}}^n$. Then f is *smooth at* $\mathbf{x}_0$ *in direction* $\boldsymbol{\xi}_0$ if there exists a neighborhood U of $\mathbf{x}_0$ and V of $\boldsymbol{\xi}_0$ such that for every $\Phi \in \mathcal{D}(U)$ and $N \in \mathbb{R}$ there exists a constant C_N such that for all $\boldsymbol{\xi} \in V$,

$$(2.1) \qquad |\mathcal{F}(\Phi f)(\lambda\boldsymbol{\xi})| \leq C_N(1+|\lambda|)^{-N}.$$

The pair $(\mathbf{x}_0, \boldsymbol{\xi}_0)$ is in the *wavefront set,* $\mathrm{WF}(f)$, if f is not smooth at $\mathbf{x}_0$ in direction $\boldsymbol{\xi}_0$.

This definition follows the intuitive idea that the elements of $\mathrm{WF}(f)$ are the point–normal vector pairs above points of X at which f has singularities. For example, if f is the characteristic function of the unit ball in $\mathbb{R}^3$, then its wavefront set is $\mathrm{WF}(f) = \{(\mathbf{x}, t\mathbf{x}) : \mathbf{x} \in S^2, t \neq 0\}$, the set of points on a sphere paired with the corresponding normal vectors to the sphere.

The wavefront set of a distribution on X is normally defined as a subset of the cotangent bundle $T^*(X)$ so it is invariant under diffeomorphisms, but we do not need this invariance, so we will continue to identify $T^*(X) = X \times \mathbb{R}^n$ and consider $\mathrm{WF}(f)$ as a subset of $X \times \dot{\mathbb{R}}^n$.

Definition 2.2 ([19, Definition 7.8.1])**.** We define $S^m(Y \times X, \mathbb{R}^N)$ to be the set of $a \in \mathcal{E}(Y \times X \times \mathbb{R}^N)$ such that for every compact set $K \subset Y \times X$ and all multi–indices α, β, γ the bound

$$\left|\partial_{\mathbf{y}}^{\gamma}\partial_{\mathbf{x}}^{\beta}\partial_{\boldsymbol{\sigma}}^{\alpha}a(\mathbf{y}, \mathbf{x}, \boldsymbol{\sigma})\right| \leq C_{K,\alpha,\beta,\gamma}(1+\|\boldsymbol{\sigma}\|)^{m-|\alpha|}, \quad (\mathbf{y}, \mathbf{x}) \in K, \ \boldsymbol{\sigma} \in \mathbb{R}^N,$$

holds for some constant $C_{K,\alpha,\beta,\gamma} > 0$.

The elements of S^m are called *symbols* of order m. Note that these symbols are sometimes denoted $S_{1,0}^m$. The symbol $a \in S^m(Y \times X, \mathbb{R}^N)$ is *elliptic* if for each compact set $K \subset Y \times X$, there is a $C_K > 0$ and $M > 0$ such that

$$(2.2) \qquad |a(\mathbf{y}, \mathbf{x}, \boldsymbol{\sigma})| \geq C_K(1+\|\boldsymbol{\sigma}\|)^m, \quad (\mathbf{y}, \mathbf{x}) \in K, \ \|\boldsymbol{\sigma}\| \geq M.$$

Definition 2.3 ([20, Definition 21.2.15])**.** A function $\Phi = \Phi(\mathbf{y}, \mathbf{x}, \boldsymbol{\sigma}) \in \mathcal{E}(Y \times X \times \dot{\mathbb{R}}^N)$ is a *phase function* if $\Phi(\mathbf{y}, \mathbf{x}, \lambda\boldsymbol{\sigma}) = \lambda\Phi(\mathbf{y}, \mathbf{x}, \boldsymbol{\sigma}), \forall\lambda > 0$ and $d\Phi$ is nowhere zero. The *critical set of* Φ is

$$\Sigma_{\Phi} = \{(\mathbf{y}, \mathbf{x}, \boldsymbol{\sigma}) \in Y \times X \times \dot{\mathbb{R}}^N : d_{\boldsymbol{\sigma}}\Phi = 0\}.$$

A phase function is *clean* if the critical set $\Sigma_{\Phi} = \{(\mathbf{y}, \mathbf{x}, \boldsymbol{\sigma}) : d_{\boldsymbol{\sigma}}\Phi(\mathbf{y}, \mathbf{x}, \boldsymbol{\sigma}) = 0\}$ is a smooth manifold with tangent space defined by the kernel of $d(d_{\boldsymbol{\sigma}}\Phi)$ on Σ_{Φ}. Here, the derivative d is applied component-wise to the vector-valued function $d_{\boldsymbol{\sigma}}\Phi$. So, $d(d_{\boldsymbol{\sigma}}\Phi)$ is treated as a Jacobian matrix of dimensions $N \times (2n + N)$.

By the Constant Rank Theorem the requirement for a phase function to be clean is satisfied if $d(d_{\boldsymbol{\sigma}}\Phi)$ has constant rank.

Definition 2.4 ([20, Definition 21.2.15] and [21, section 25.2]). Let X and Y be open subsets of $\mathbb{R}^n$. Let $\Phi \in \mathcal{E}\left(Y \times X \times \mathbb{R}^N\right)$ be a clean phase function. In addition, we assume that Φ is *nondegenerate* in the following sense:

$$\mathrm{d}_{\mathbf{y}}\Phi \text{ and } \mathrm{d}_{\mathbf{x}}\Phi \text{ are never zero on } \Sigma_\Phi.$$

The *canonical relation parametrized by* Φ is defined as

(2.3) $$\mathcal{C} = \{((\mathbf{y}, \mathrm{d}_{\mathbf{y}}\Phi(\mathbf{y}, \mathbf{x}, \boldsymbol{\sigma})) ; (\mathbf{x}, -\mathrm{d}_{\mathbf{x}}\Phi(\mathbf{y}, \mathbf{x}, \boldsymbol{\sigma}))) : (\mathbf{y}, \mathbf{x}, \boldsymbol{\sigma}) \in \Sigma_\Phi\},$$

Definition 2.5. Let X and Y be open subsets of $\mathbb{R}^{n_X}$ and $\mathbb{R}^{n_Y}$, respectively. Let an operator $A : \mathcal{D}(X) \to \mathcal{D}'(Y)$ be defined by the distribution kernel $K_A \in \mathcal{D}'(Y \times X)$, in the sense that $Af(\mathbf{y}) = \int_X K_A(\mathbf{y}, \mathbf{x})f(\mathbf{x})\mathrm{d}\mathbf{x}$. Then we call K_A the *Schwartz kernel* of A. A *Fourier integral operator (FIO)* of order $m + N/2 - (n_X + n_Y)/4$ is an operator $A : \mathcal{D}(X) \to \mathcal{D}'(Y)$ with Schwartz kernel given by an oscillatory integral of the form

(2.4) $$K_A(\mathbf{y}, \mathbf{x}) = \int_{\mathbb{R}^N} e^{i\Phi(\mathbf{y}, \mathbf{x}, \boldsymbol{\sigma})} a(\mathbf{y}, \mathbf{x}, \boldsymbol{\sigma})\mathrm{d}\boldsymbol{\sigma},$$

where Φ is a clean nondegenerate phase function and a is a symbol in $S^m(Y \times X, \mathbb{R}^N)$. The *canonical relation of* A is the canonical relation of Φ defined in (2.3). The FIO A is *elliptic* if its symbol is elliptic.

This is a simplified version of the definition of FIOs in [8, section 2.4] or [21, section 25.2] that is suitable when there are global coordinates and a global phase function. Definition 2.5 provides some of the mathematical tools we need to analyze image artifacts in important imaging applications, such as URT, and thus the simplified definition we use here is well-motivated. In general, an FIO must be defined using a partition of unity, local coordinates, and phase functions corresponding to local regions of the same, globally defined, canonical relation; for details see [8, section 2.4] or [21, section 25.2]. Because we assume phase functions are nondegenerate, our FIOs can be defined as maps from $\mathcal{E}'(X)$ to $\mathcal{D}'(Y)$ and sometimes on larger domains. For general information about FIOs, see [8, 21, 20]. For information about the Schwartz Kernel, see [19, Theorem 5.1.9].

Pseudodifferential operators are a special class of FIOs, which include linear differential operators, given in the next definition.

Definition 2.6. An FIO is a pseudodifferential operator if its canonical relation $\mathcal{C}$ is contained in the diagonal

$$\mathcal{C} = \Delta := \{(\mathbf{x}, \boldsymbol{\xi}; \mathbf{x}, \boldsymbol{\xi})\}.$$

Let X and Y be sets and let $\Omega_1 \subset X$ and $\Omega_2 \subset Y \times X$. The composition $\Omega_2 \circ \Omega_1$ and transpose Ω_2^t of Ω_2 are defined

$$\Omega_2 \circ \Omega_1 = \{\mathbf{y} \in Y : \exists \mathbf{x} \in \Omega_1, \ (\mathbf{y}, \mathbf{x}) \in \Omega_2\}$$
$$\Omega_2^t = \{(\mathbf{x}, \mathbf{y}) : (\mathbf{y}, \mathbf{x}) \in \Omega_2\}.$$

The Hörmander-Sato Lemma provides the relationship between the wavefront set of distributions and their images under FIOs.

Theorem 2.7 ([19, Theorem 8.2.13]). *Let* $f \in \mathcal{E}'(X)$ *and let* $A : \mathcal{E}'(X) \to \mathcal{D}'(Y)$ *be an FIO with canonical relation* $\mathcal{C}$. *Then,* $\mathrm{WF}(Af) \subset \mathcal{C} \circ \mathrm{WF}(f)$.

Let A be an FIO with adjoint A^*. Then if $\mathcal{C}$ is the canonical relation of A, the canonical relation of A^* is $\mathcal{C}^t$. Many imaging techniques are based on application of the adjoint operator A^* and so to understand artifacts we consider A^*A (or, if A does not map to $\mathcal{E}'(Y)$, then $A^*\psi A$ for an appropriate cutoff ψ). Because of Theorem 2.7,

$$\mathrm{WF}(A^*\psi A f) \subset \mathcal{C}^t \circ \mathcal{C} \circ \mathrm{WF}(f).$$

The next two definitions provide tools, which we will apply in the next section, to analyze this composition.

Definition 2.8. Let $\mathcal{C} \subset T^*(Y \times X)$ be the canonical relation associated to the FIO $A : \mathcal{E}'(X) \to \mathcal{D}'(Y)$. We let Π_L and Π_R denote the natural left- and right-projections of $\mathcal{C}$, projecting onto the appropriate coordinates: $\Pi_L : \mathcal{C} \to T^*(Y)$ and $\Pi_R : \mathcal{C} \to T^*(X)$.

Because Φ is nondegenerate, the projections do not map to the zero section. If A satisfies our next definition, then A^*A (or $A^*\psi A$) is a pseudodifferential operator [16, 29].

Definition 2.9. Let $A : \mathcal{E}'(X) \to \mathcal{D}'(Y)$ be a FIO with canonical relation $\mathcal{C}$ then A (or $\mathcal{C}$) satisfies the *Bolker Condition* if the natural projection $\Pi_L : \mathcal{C} \to T^*(Y)$ is an embedding (injective immersion).

3. Ellipsoid and hyperboloid Radon transforms

In this section we show under fairly weak assumptions that a general Radon transform integrating over ellipsoids, hyperboloids, or elliptic hyperboloids with centers on a surface satisfies the Bolker condition. Then, we investigate several special cases.

Let $\mathrm{Sym}(n)$ denote the set of invertible symmetric matrices with real entries, which is an $n(n+1)/2$ dimensional smooth manifold, and suppose $A \in \mathrm{Sym}(n)$. Let S be a smooth connected hypersurface in $\mathbb{R}^n$. For $(\mathbf{s}, A, t) \in S \times \mathrm{Sym}(n) \times \mathbb{R} =: Y$, let

$$(3.1) \qquad \Psi(\mathbf{s}, A, t; \mathbf{x}) = t - \mathbf{x}_T^T A \mathbf{x}_T \quad \text{where} \quad \mathbf{x}_T = \mathbf{x} - \mathbf{s}.$$

If A is positive definite and $t > 0$, then $\Psi(\mathbf{s}, A, t; \mathbf{x}) = 0$ is the defining equation of an ellipsoid with center at $\mathbf{s}$. In other cases, $\Psi(\mathbf{s}, A, t; \mathbf{x}) = 0$ can be a hyperboloid or elliptic hyperboloid. Note that if $t = 0$, the surface $\Psi(\mathbf{s}, A, 0; \mathbf{x}) = 0$ is singular. Therefore, we will exclude $t = 0$ from our analysis.

Our Radon transform can be written

$$(3.2) \qquad \begin{aligned} Rf(\mathbf{s}, A, t) &= \int_{\mathbb{R}^n} |\nabla_{\mathbf{x}}\Psi|\, \delta\left(\Psi(\mathbf{s}, A, t; \mathbf{x})\right) f(\mathbf{x}) \mathrm{d}\mathbf{x} \\ &= \int_{-\infty}^{\infty} \int_{\mathbb{R}^n} |\nabla_{\mathbf{x}}\Psi|\, f(\mathbf{x}) e^{i\sigma \Psi(\mathbf{s}, A, t; \mathbf{x})} \mathrm{d}\mathbf{x}\mathrm{d}\sigma \end{aligned}$$

for $f \in L_c^2(D)$, where D is an open, connected subset of $\mathbb{R}^n$. The weight, $|\nabla_{\mathbf{x}}\Psi|$, is included so that R defines surface integrals with respect to the surface elements on ellipsoids and hyperboloids, in line with the theory of Palamodov [27]. The most general case we will consider is when A is restricted to be in an embedded submanifold $M \subset \mathrm{Sym}(n)$. Note that this includes the case when $M = \{A\}$ is a single matrix and thus a zero dimensional submanifold. With this in mind, we define

$$Y_M = S \times M \times \dot{\mathbb{R}}$$

and the operator R_M is given by (3.2) but with A restricted to M.

We now state our main theorem.

Theorem 3.1. *Let $S \subset \mathbb{R}^n$ be a smooth connected hypersurface. Let D be an open connected subset of $\mathbb{R}^n$, and let M be a submanifold of $\mathrm{Sym}(n)$, possibly of dimension zero. Then, $R_M : \mathcal{E}'(D) \to \mathcal{D}'(Y_M)$ is an FIO satisfying the Bolker condition if D is disjoint from every tangent plane to S. That is,*

$$(3.3) \qquad D \cap \left(\bigcup_{\mathbf{s} \in S} P_{\mathbf{s}} \right) = \emptyset,$$

where $P_\mathbf{s}$ is the tangent plane to S at $\mathbf{s} \in S$. If additionally $\dim(M) = 0$, then the Bolker condition will fail if any tangent plane to S intersects D.

We should point out that Theorem 3.1 will apply to the Radon transform R_M with any smooth weight, not just the weight in (3.2), since the proof uses only microlocal results related to the phase function, and the symbol of R_M will still be smooth.

In the proof of Theorem 3.1 and throughout the article, we use the following notation: $\mathbf{0}_{m \times n}$ is the $m \times n$ zero matrix; and I_m is the $m \times m$ identity matrix. If $\mathbf{x} = (x_1, x_2, \ldots, x_{n-1}, x_n) \in \mathbb{R}^n$, then $\mathbf{x}' = (x_1, x_2, \ldots, x_{n-1})$.

Proof of Theorem 3.1. Referring to the second line in (3.2), R_M will be an FIO provided that

$$(3.4) \qquad \Phi(\mathbf{s}, A, t; \mathbf{x}; \sigma) = \sigma \left(t - \mathbf{x}_T^T A \mathbf{x}_T \right)$$

is a nondegenerate phase function. This is true since $\frac{\partial \Phi}{\partial t} = \sigma$ and $\nabla_\mathbf{x} \Phi = -2\sigma(A\mathbf{x}_T)^T \neq \mathbf{0}$ since D is disjoint from S and A is invertible.

Our main proof is in two parts. First we consider the case when S is the graph of a smooth function, and then we use this result locally for the general case. We will first assume $\dim(M) > 0$ and deal with $\dim(M) = 0$ at the end. Indeed, let Ω be an open connected subset of $\mathbb{R}^{n-1}$ and let $q : \Omega \to \mathbb{R}$ be a smooth function. Now, let

$$S = \{ (\mathbf{y}, q(\mathbf{y})) : \mathbf{y} \in \Omega \}.$$

To simplify notation when $\mathbf{y} \in \Omega$ is fixed, we will let

$$q = q(y_1, \ldots, y_{n-1}), \qquad q_j = \frac{\partial q}{\partial y_j}$$

and so for $\mathbf{x} \in \mathbb{R}^n$, $\mathbf{y} \in \Omega$

$$\mathbf{x}_T = (x_1 - y_1, x_2 - y_2, \ldots, x_{n-1} - y_{n-1}, x_n - q)^T.$$

Note that, with this notation, $\mathbf{x}$ is in the tangent plane $P_{(\mathbf{y}, q(\mathbf{y}))}$ if and only if

$$(3.5) \qquad (\nabla q^T, -1) \cdot \mathbf{x}_T = (q_1, \ q_2, \ \ldots, \ q_{n-1}, \ -1) \cdot \mathbf{x}_T = 0.$$

When $\dim(M) > 0$, a calculation using (3.4) shows that the canonical relation for R_M is

$$(3.6) \qquad \begin{aligned} \mathcal{C}_M = \big\{ \big((\mathbf{y}, q), A, \mathbf{x}_T^T A \mathbf{x}_T; \nabla_\mathbf{y} \Phi \cdot \mathrm{d}\mathbf{y} + \nabla_A \Phi \cdot \mathrm{d}A + \sigma \mathrm{d}t; \mathbf{x}; -\nabla_\mathbf{x} \Phi \cdot \mathrm{d}\mathbf{x} \big) \\ : (\mathbf{y}, A; \mathbf{x}; \sigma) \in \Omega \times M \times D \times \dot{\mathbb{R}} \big\} \end{aligned}$$

The only difference when $\dim(M) = 0$ is that the $\mathrm{d}A$ term is removed.

7

Note that $(\mathbf{y}, A; \mathbf{x}; \sigma) \in \Omega \times M \times D \times \dot{\mathbb{R}}$ provide a global parametrization of $\mathcal{C}_M$ since t is determined by $\mathbf{y}$, $q(\mathbf{y})$, $\mathbf{x}$ and A. The left projection of R_M is

$$(3.7) \qquad \Pi_L^M(\mathbf{y}, A; \mathbf{x}; \sigma) = \left((\mathbf{y}, q), A, \mathbf{x}_T^T A \mathbf{x}_T; 2\sigma \mathbf{x}_T^T A B^T \cdot d\mathbf{y} - \sigma \mathbf{x}_T^T \cdot dA\mathbf{x}_T + \sigma \cdot dt \right),$$

where

$$B = [I_{n-1}, \nabla q] = \begin{pmatrix} 1 & 0 & \cdots & 0 & q_1 \\ 0 & 1 & \cdots & 0 & q_2 \\ \vdots & \vdots & \vdots & \vdots & \vdots \\ 0 & 0 & \cdots & 1 & q_{n-1} \end{pmatrix}.$$

Note that we do not need to calculate the dA term in the projection because we will show Bolker holds under our restrictions on the connected open set D just using the other terms in (3.7). Using the natural coordinates on $T^*(\Omega \times M \times \dot{\mathbb{R}})$, the differential of Π_L^M is represented by

$$(3.8) \qquad D\Pi_L^M = \begin{matrix} & \overset{\nabla_{\mathbf{y}}, \nabla_A, \frac{\partial}{\partial \sigma}}{} & \overset{\nabla_{\mathbf{x}}}{} \\ \begin{matrix} \mathbf{y}, A, dt \\ d\mathbf{y} \\ dA \\ t \end{matrix} & \begin{pmatrix} I_{(2n-1)} & \mathbf{0}_{(2n-1)\times n} \\ \cdot & 2\sigma BA \\ \cdot & \cdot \\ \cdot & 2\mathbf{x}_T^T A \end{pmatrix} \end{matrix}.$$

Thus, Π_L^M will be an immersion if the $n \times n$ submatrix

$$(3.9) \qquad C = \begin{pmatrix} 2\sigma BA \\ 2\mathbf{x}_T^T A \end{pmatrix} = \begin{pmatrix} 2\sigma B \\ 2\mathbf{x}_T^T \end{pmatrix} A$$

is invertible. Note that CA^{-1} is row equivalent to

$$(3.10) \qquad (CA^{-1})' = \begin{pmatrix} I_{n-1} & \nabla q \\ \mathbf{0}_{1\times(n-1)} & (\nabla q^T, -1) \cdot \mathbf{x}_T \end{pmatrix}.$$

Therefore, by (3.5) $D\Pi_L^M$ is injective if $\mathbf{x}$ is not on the tangent plane to S at $(\mathbf{y}, q)$.

Now we will prove the injectivity part of the Bolker condition when S is a graph assuming that D is connected and (3.3) holds.

Seeking to establish injectivity, let us suppose that $\mathbf{u}, \mathbf{v} \in D$, $A \in M$ and $\sigma \in \dot{\mathbb{R}}$ are such that

$$(3.11) \qquad \Pi_L^M(\mathbf{y}, A; \mathbf{u}; \sigma) = \Pi_L^M(\mathbf{y}, A; \mathbf{v}; \sigma).$$

Then, using (3.7), we see

$$(3.12) \qquad BA\mathbf{u}_T = BA\mathbf{v}_T.$$

Note that $\text{Null}(BA) = \text{span}\left(A^{-1}(-\nabla q^T, 1)^T \right)$ and because of (3.12)

$$(3.13) \qquad \mathbf{u}_T = \mathbf{v}_T + sA^{-1}(-\nabla q^T, 1)^T.$$

for some $s \in \mathbb{R}$. On the other hand, by setting the t components in (3.7) equal we have

$$(3.14) \qquad \mathbf{u}_T^T A \mathbf{u}_T = \mathbf{v}_T^T A \mathbf{v}_T$$

By taking the inner product of (3.13) with $A\mathbf{u}_T$ and using (3.14), we see that

$$(3.15) \qquad -s\mathbf{v}_T \cdot (-\nabla q^T, 1)^T = s\mathbf{u}_T \cdot (-\nabla q^T, 1)^T.$$

8

Let $P_{\mathbf{s}}$ be the tangent plane to S at $\mathbf{s} = (\mathbf{y}, q)$. There are three possibilities for (3.15) to be valid. If $s = 0$, then $\mathbf{u} = \mathbf{v}$. If $(-\nabla q^T, 1)^T \cdot \mathbf{v}_T = 0$ or $(-\nabla q^T, 1)^T \cdot \mathbf{u}_T = 0$, then both $\mathbf{v}$ and $\mathbf{u}$ are in $P_{\mathbf{s}}$, but this is excluded. In the third case, $\mathbf{v}_T \cdot (-\nabla q^T, 1)^T$ and $\mathbf{u}_T \cdot (-\nabla q^T, 1)^T$ have opposite signs and so $\mathbf{u}$ and $\mathbf{v}$ are on opposite sides of the tangent plane. Since D is connected, open and disjoint from every tangent plane to S, this last case is not possible.

In the proof up to now, we did not consider the $\mathrm{d}A$ term in Π_L^M (see (3.7)). Therefore, if $\dim(M) > 0$ then the $\mathrm{d}A$ term could cause Π_L^M to be injective and/or an immersion, even if D does not satisfy our hypotheses. This is why the theorem is not an equivalence in general.

Now, assume $\dim(M) = 0$. In this case, the $\mathrm{d}A$ term does not appear in (3.7). So, the rows of (3.8) corresponding to $\mathrm{d}A$ in (3.8) are absent and therefore $D\Pi_L^M$ is injective if and only if $\mathbf{x}$ is not in the tangent plane $P_{\mathbf{s}}$ to S at $\mathbf{s} = (\mathbf{y}, q)$. Therefore, if the Bolker condition holds, then $D\Pi_L^M$ must be an immersion above all $\mathbf{s} \in S$, and (3.3) holds.

With this case handled, we now assume that S is an arbitrary imbedded hypersurface in $\mathbb{R}^n$ and we assume D is connected and open and no tangent plane to S intersects D. Let $\mathbf{s}_0 \in S$. We will show that Π_L^M is an injective immersion locally above S near $\mathbf{s}_0$ (i.e., on the canonical relation $\mathcal{C}_M$ and above points $(\mathbf{s}, A, t) \in Y_M$ for $\mathbf{s}$ in a neighborhood in S of $\mathbf{s}_0$). We do this by reducing the problem to the case we just considered, when the hypersurface S is a graph.

This will show $R_M : \mathcal{E}'(D) \to \mathcal{D}'(Y_M)$ satisfies the Bolker assumption globally for the following reasons. First, being an immersion is a local condition. To check injectivity, note that if $\Pi_L^M(\nu_0) = (\mathbf{s}_0, A_0, t_0; \eta_0) = \Pi_L^M(\nu_1)$ then, since the basepoints of the image are the same, to show $\nu_0 = \nu_1$, one just needs to know Π_L^M is injective on $\left(\Pi_L^M\right)^{-1} \{(\mathbf{s}_0, A_0, t_0; \eta_0)\}$.

Using a translation T of $\mathbb{R}^n$ followed by a rotation R we map $\mathbf{s}_0$ into $\mathbf{0} \in \mathbb{R}^n$ and S into a connected submanifold S' such that the hyperplane $P_{\mathbf{0}} = \{\mathbf{x} \in \mathbb{R}^n : x_n = 0\}$ is tangent to S' at $\mathbf{s} = \mathbf{0}$. We let D' be the image of D under this rigid motion, RT. Without loss of generality, we assume that D' is above $P_{\mathbf{0}}$. The rotation R also conjugates M to another embedded manifold in $\mathrm{Sym}(n)$, which we denote by M'.

Let Ω be an open connected neighborhood of $\mathbf{0} \in \mathbb{R}^{n-1}$ that is so small that there is a smooth function $q : \Omega \to [0, \infty)$ such that

$$\Omega \ni \mathbf{y} \mapsto (\mathbf{y}, q(\mathbf{y}))$$

give local coordinates on S' near $\mathbf{0}$. Let

$$S_0' = \{(\mathbf{y}, q(\mathbf{y})) : \mathbf{y} \in \Omega\} .$$

Since D' is above $P_{\mathbf{0}}$, it is above every tangent plane to S_0' by the Intermediate Value Theorem argument given earlier.

Let $Y_0' = \left\{(\mathbf{y}, q(\mathbf{y})), A, t) : \mathbf{y} \in \Omega, A \in M', t \in \dot{\mathbb{R}}\right\}$. Since D' is disjoint from every tangent plane to S_0', the first part of this proof implies that $R_{M'} : \mathcal{E}'(D') \to \mathcal{D}'(Y_0')$ satisfies the Bolker condition. Let S_0 be the image of S_0' under $(RT)^{-1}$ and let $Y_0 = S_0 \times M \times \dot{\mathbb{R}}$. This proof implies that $R_M : \mathcal{E}'(D) \to \mathcal{D}'(Y_0)$ satisfies the Bolker condition. Since the Bolker condition is local above Y_M and these coordinate patches cover S, the Bolker condition holds for $R_M : \mathcal{E}'(D) \to \mathcal{D}'(Y_M)$.

This finishes the proof. $\qquad\square$

3.1. **Visible singularities and artifacts.** The normal operator for R_M is $\mathcal{N} = R_M^* \varphi R_M$ where φ is a cutoff on Y_M that guarantees one can compose these operators, and if R_M is a proper map, the cutoff φ is not needed. A backprojection operator is one of the form $R_M^\dagger P R_M$ for some properly supported pseudodifferential operator P and $R_M^\dagger$ is a smoothly weighted adjoint (the backprojection).

Visible singularities of f are those that are singularities of $\mathcal{N}f$, i.e., singularities in $\mathrm{WF}(\mathcal{N}f) \cap \mathrm{WF}(f)$. Other singularities of f are called *invisible singularities*. *Artifacts* are singularities of $\mathcal{N}f$ that are not in f, i.e., singularities in $\mathrm{WF}(\mathcal{N}f) \setminus \mathrm{WF}(f)$.

To understand visible singularities, note that the set of visible singularities of f is contained in the image of $\Pi_R^M(\mathcal{C}_M)$. This is true because

$$(3.16) \qquad \mathrm{WF}(\mathcal{N}f) \subset \mathcal{C}_M^t \circ \mathcal{C}_M \circ \mathrm{WF}(f) = \Pi_R^M \circ \left(\Pi_L^M\right)^{-1} \circ \Pi_L^M \circ \left(\Pi_R^M\right)^{-1}(\mathrm{WF}(f)),$$

by the Hörmander-Sato Lemma [19, Theorem 8.2.13] and so the only singularities that will come from this composition will be those in $\Pi_M^R(\mathcal{C}_M)$.

Now, we consider visible singularities for the spherical transform, so $M = \{I_n\}$. We claim, there will be more visible singularities the more S "wraps around" the scanning region. To see this, one first observes that a singularity $(\mathbf{x}, \xi) \in \mathrm{WF}(f)$ is detected by spherical integrals only if $\{\mathbf{x} + \alpha\xi : \alpha \in \mathbb{R}\} \cap S \neq \emptyset$. This follows by a calculation of $\mathcal{C}_M$ for this case (either use the expression for $\mathcal{C}_M$ in (3.6) for the spherical case and then find the image of $\Pi_R^M(\mathcal{C}_M)$ or see e.g., the discussion of visible singularities around (4.6) and (4.13) in [13]). Therefore, if S is as in Figure 3b, then $R_M f$ detects all singularities in D since S surrounds D. If S is as in Figure 3c, then singularities in a horizontal direction at points above S are invisible since no horizontal line through such points intersects S.

We now discuss possible microlocal artifacts when Π_L^M is not injective. Let $(\mathbf{s}, A, t) \in Y_M$. Assume $\mathbf{u}$ and $\mathbf{v}$ are distinct points in D such that

$$(3.17) \qquad \Pi_L^M(\mathbf{s}, A, t; \mathbf{u}; \sigma) = \Pi_L^M(\mathbf{s}, A, t; \mathbf{v}; \sigma).$$

Let $E = \{\mathbf{x} \in \mathbb{R}^n : \Psi(\mathbf{s}, A, t; \mathbf{x}) = 0\}$ be the hypersurface that $R_M f(\mathbf{s}, A, t)$ integrates over and let $P_\mathbf{s}$ be the tangent plane to S at $\mathbf{s}$. Note that $\mathbf{u}$ and $\mathbf{v}$ must be in E by (3.17) and the definition of C_M.

If $A^{-1}(-\nabla q^T, 1)^T$ is not parallel $P_\mathbf{s}$, then, by the assumption (3.17) and the proof using (3.13)-(3.15), $\mathbf{u}$ and $\mathbf{v}$ are on opposite sides of $P_\mathbf{s}$. If $A^{-1}(-\nabla q^T, 1)^T$ is parallel to $P_\mathbf{s}$, then $\mathbf{u}$ and $\mathbf{v}$ are on $E \cap P_\mathbf{s}$. In both cases, we will call $\mathbf{u}$ and $\mathbf{v}$ mirror points. By the Hörmander Sato Lemma and the non-injectivity of Π_L^M, a singularity at $\mathbf{u}$ conormal to E can be reflected to an added artifact at the mirror point $\mathbf{v}$ that is conormal to E under the normal operator, $R_M^t \varphi R_M$ or other backprojection type operators. This point $\mathbf{v}$ comes about through our microlocal results (see (3.15)).

It may be possible to further analyze the normal operator microlocally by examining points where $D\Pi_L^M$ drops rank as done for other cases in, for example, [10, 11, 26, 34, 36] but this is reserved for future work. By the proof of Theorem 3.1, in particular formula (3.15), the rank can only drop if $\mathbf{u} \in P_\mathbf{s}$ since otherwise Π_L^M is locally injective.

3.2. **Examples.** In this section, we apply Theorem 3.1 to several interesting special cases.

Corollary 3.2. *Let C be an open convex set with a smooth boundary, S, and let M be a submanifold of $\mathrm{Sym}(n)$, possibly of dimension zero. Then, $R_M : \mathcal{E}'(C) \to \mathcal{D}'(Y_M)$ is an FIO satisfying the Bolker condition.*

The corollary follows because condition (3.3) in Theorem 3.1 holds as C is convex and S is smooth.

Example 3.3 (S with gradient zero along an axis). In this example, we consider measurement surfaces S which are flat along one directional axis, and the special case when the integral surfaces are ellipsoids of revolution (or spheroids). Without loss of generality, in this example, S is assumed to be flat in the x_{n-1} direction. In Ultrasound reflection tomography (URT), the integration surfaces are spheroids, and the foci of the spheroids represent the sound wave emitter/receiver positions [2]. If we were to construct a measurement surface in URT, which is flat in the x_{n-1} direction, such that there is an emitter/receiver at every point on S (i.e., we have an $(n-1)$-D surface of emitters), then the URT data can be modeled by Rf, where f, in URT, denotes the acoustic reflectivity function. Specifically, we set $A = \text{diag}(1,\ldots,1,r_{n-1},1)$ in equation (3.1), with $r_{n-1} \in (0,1]$, and constrain S to have gradient zero in the x_{n-1} direction. Then the defining function, Ψ (see section 3, equation (3.1)), describes a spheroid surface with foci on S. Thus, Theorem 3.1 has direct applications to measurement surfaces in URT.
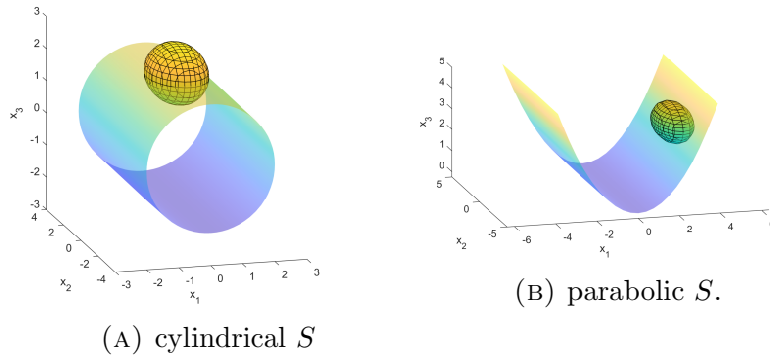

(A) cylindrical S

(B) parabolic S.

FIGURE 1. Example S in $\mathbb{R}^3$ with practical application to URT. The surfaces above are flat (gradient zero) in the x_2 direction and are globally convex.

In Figure 1, we have illustrated some example $S \subset \mathbb{R}^3$, which are flat in the x_2 direction, and for which the Bolker condition holds. In Figure 1a, the function support lies in the cylinder interior, and in Figure 1b, the function support is assumed to be contained in $\{x_3 > x_1^2\}$.

Example 3.4 (Centers on a hyperplane). Integral transforms over spheres or ellipsoids centered on a plane have been studied for application to radar [34, 5, 23, 6], sonar [4, 22], seismic [15], and ultrasound imaging [2, 14]. Theorem 3.1 holds if S is a hyperplane and D is on one side of S. Note that this does not cover the common offset geometry, where integrals are being taken over ellipsoids centered on a plane and with foci a fixed distance apart, or common midpoint, where integrals are being taken over ellipsoids with foci symmetric about a line cases considered in [12] where integrals are being taken over ellipsoids with foci a fixed distance apart and oriented for each $\mathbf{y} \in S$, since the foci of our ellipses change with t.

Example 3.5 (Centers on a spheroid, exponential, and sinusoid surface). In this example, we discuss additional example measurement surfaces in cases when the Bolker condition is satisfied, and others when Bolker is not satisfied. Specifically, we consider the spheroid and

(A) ellipsoid centered on flat plane

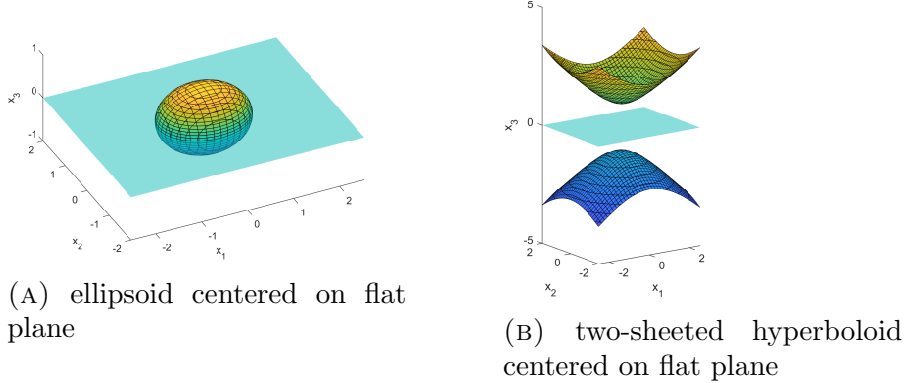(B) two-sheeted hyperboloid centered on flat plane

FIGURE 2. Flat plane measurement surface. Left - ellipsoid integral surface. Right - two-sheeted hyperboloid surface.

exponential surfaces illustrated in Figures 3a and 3b. In Figure 3a, the function support is assumed to be contained within the spheroid interior, and in Figure 3b, $S = \{\mathbf{x} \in \mathbb{R}^3 : x_3 - e^{x_1^2 + x_2^2} = 0\}$, and $\text{supp}(f) \subset \{x_3 > e^{x_1^2 + x_2^2}\}$. In both cases, no plane tangent to S intersects $\text{supp}(f)$. Therefore, Theorem 3.1 holds.

In Figure 3c, we give an example "sinusoidal" measurement surface, defined by $S = \{\mathbf{x} \in \mathbb{R}^3 : x_3 - \sin x_1 + \sin x_2 = 0\}$, with $\text{supp}(f) \subset \{\mathbf{x} \in \mathbb{R}^3 : x_3 - \sin x_1 + \sin x_2 > 0\}$. In this case, there exist planes tangent to S which intersect $\text{supp}(f)$, and thus, if $\dim(M) = 0$, the Bolker condition is not satisfied by Theorem 3.1, and we would expect to see mirror-point type artifacts through planes tangent to S, as described in section 3.1.

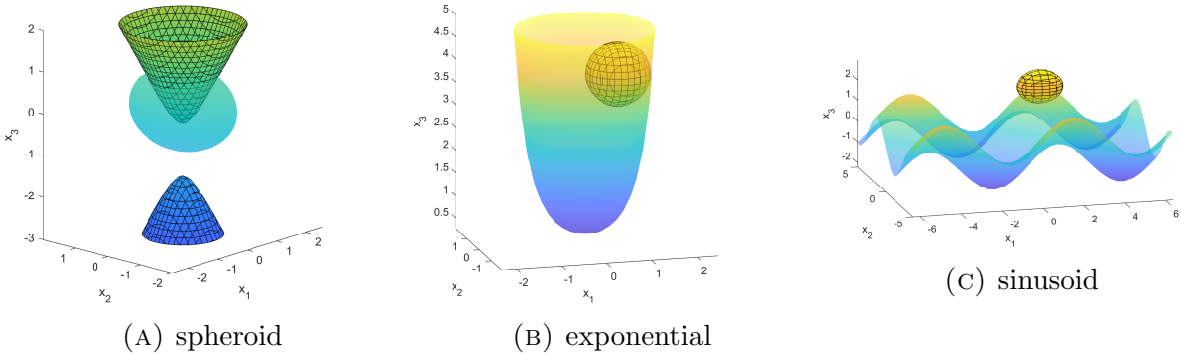(A) spheroid

(B) exponential

(C) sinusoid

FIGURE 3. Two-sheeted hyperboloid and ellipsoid surfaces of integration centered on convex and non-convex scanning surfaces. In (3c) so Bolker is not satisfied (see section 3.1).

4. CYLINDRICAL MEASUREMENT SURFACE IN $\mathbb{R}^3$

In this section, we investigate in more detail the cylindrical scanning surface introduced in Example 3.3 and Figure 1a. Specifically, we show that any L^2 function, with compact support on a cylinder interior, can be recovered uniquely from its integrals over spheroids with foci on a cylinder. We also discuss in more detail the visible singularities and how the stability varies with the discretization of emitters/receivers on the cylinder surface.

Our center set will be the cylinder of radius one with axis parallel to the second coordinate axis and we will consider spheroids with rotation axis on C, centers

$$(4.1) \qquad \mathbf{s} = \mathbf{s}(\phi_0, y_0) = (\cos\phi_0, y_0, \sin\phi_0)^T \in C,$$

and fixed aspect ratio $s \in (0, 1]$. This gives the Radon transform

$$(4.2) \qquad R_s f(p, \phi_0, y_0) = Rf\left(\mathbf{s}(\phi_0, y_0), \operatorname{diag}(1, s^2, 1), p^2\right),$$

where t is replaced by $p^2 = t$ in (3.1).

In the following subsections, we address the injectivity and microlocal stability properties of R_s.

Remark 4.1. Injectivity results are proven in [18], for a class of generalized Radon transforms for real-analytic submanifolds in a compact real-analytic manifold with boundary. This important work does not imply injectivity for R_s for reasons which we now explain. The key point is that the spheroids R_s integrates over are not parameterized as in [18]. After a reduction, the authors in [18] parameterize their manifolds of integration by $(s, \theta) \in \mathbb{R} \times S^{n-1}$ [18, p. 1518], but our spheroids are parameterized by $(p, \mathbf{s}) \in \mathbb{R} \times C$. C is topologically neither compact nor simply connected, although S^{n-1} is. Thus, the theory of [18] cannot apply to R_s. To prove injectivity for R_s, we apply linear Volterra equation theory. We also provide an inversion method based on Neumann series.

4.1. **Injectivity.** We first introduce notation we will use in the proofs and define the auxiliary variables

$$(4.3) \quad \hat{x}_1 = \hat{x}_1(\phi_0, x_1, x_3) = \sqrt{(x_1 - \cos\phi_0)^2 + (x_3 - \sin\phi_0)^2} \qquad \hat{x}_2 = \hat{x}_2(x_2, y_0) = x_2 - y_0,$$

then $\hat{x}_1$ represents the radius of the circle in Figure 4. In this notation, we can describe the spheroid defined by matrix $M = \operatorname{diag}(1, s^2, 1)$, center $\mathbf{s}(\phi_0, y_0)$, and parameter p as

$$(4.4) \qquad \hat{x}_1^2 + s^2 \hat{x}_2^2 = p^2.$$

We use standard cylindrical coordinates for points inside C:

$$\mathbf{x} = (x_1, x_2, x_3) = (r\cos\phi, x_2, r\sin\phi), \quad \text{where} \ \ r > 0 \ \ \phi \in [0, 2\pi].$$

In this notation the polar radius for $\mathbf{x}$ is

$$(4.5) \qquad r = \sqrt{\hat{x}_1^2 + 1 - 2\hat{x}_1\cos\theta}, \quad \hat{\phi} = \phi - \phi_0, \quad \frac{\hat{x}_1}{\sin\hat{\phi}} = \frac{r}{\sin\theta},$$

where $\hat{\phi}$ is the angle between (x_1, x_3) and $(\cos\phi_0, \sin\phi_0)$. See Figure 4. Note that Figure 4 shows the picture for $\phi_0 = 0$ and, in general, the picture is rotated and $\hat{\phi}$ is measured from the vector $(\cos\phi_0, \sin\phi_0)$.

We use Figures 4 and 5 in the proofs to explain the geometry behind our integrals. They show two cross-sections of the spheroid (4.4) with center $\mathbf{s}(0, y_0) = (1, y_0, 0)$: first with a plane perpendicular to the x_2 axis in Figure 4 and second with a plane containing the axis of the cylinder and $\mathbf{s}$ in Figure 5.

The following proposition is the first step in writing $R_s f$ in terms of Volterra equations of Fourier coefficients of f.
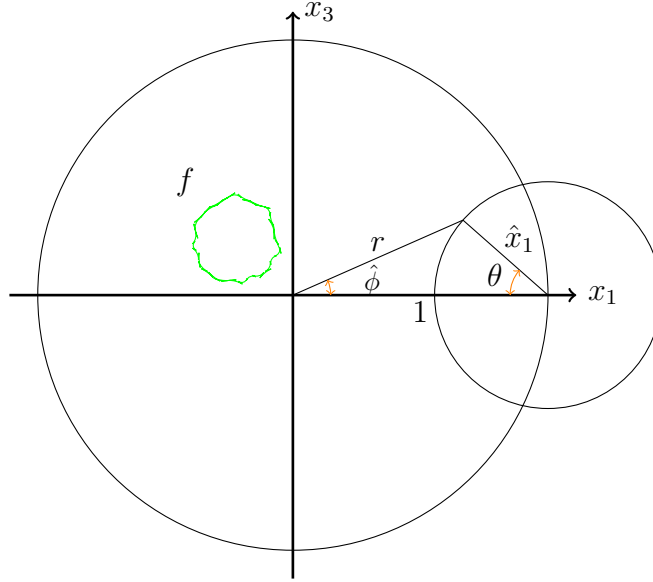
FIGURE 4. A cross section of the spheroid with center $(1, 0, 0) = \mathbf{s}(0, 0)$ perpendicular to the spheroid axis at $\hat{x}_2 = x_2$. The axes are (x_1, x_3) because $\phi_0 = 0$ but the picture would be rotated for general ϕ_0 and then the angle $\hat{\phi}$ would be measured from the ray containing $(\cos \phi_0, \sin \phi_0)$. The cylinder has unit radius.
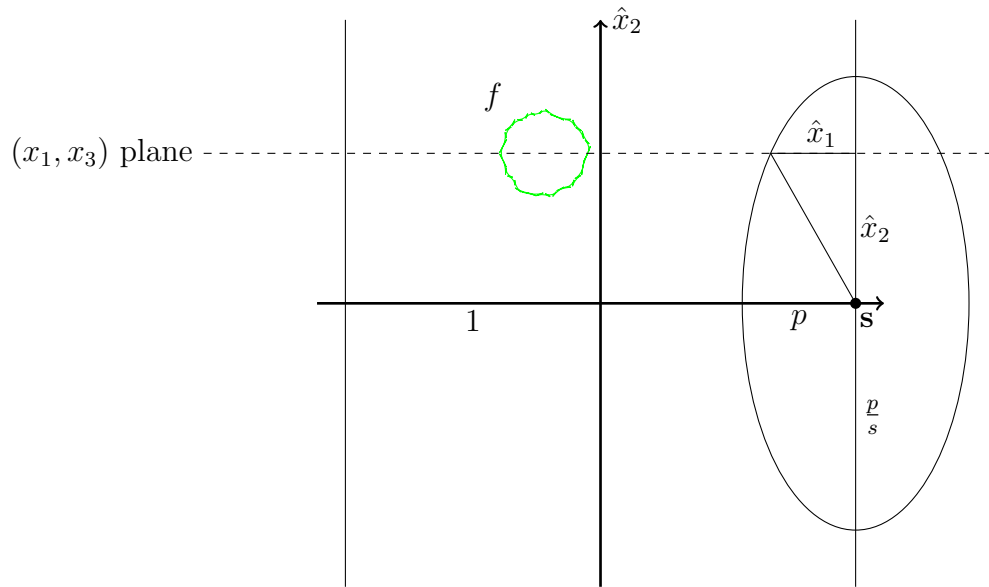

FIGURE 5. Cylindrical geometry $(\hat{x}_1, \hat{x}_2)$ plane cross section. The (x_1, x_3) plane of Figure 4 is drawn as a dashed line.

Proposition 4.2. Let $f \in L^2_c(\mathbb{R}^3)$. Then
(4.6)
$$
R_s f(p, \phi_0, y_0) = \int_{-\frac{p}{s}}^{\frac{p}{s}} \sqrt{p^2 - s^2 \hat{x}_2^2 + s^4 \hat{x}_2^2} \int_{-\pi}^{\pi} f\left(r, \sin^{-1}\left(\frac{\hat{x}_1}{r} \sin \theta\right) + \phi_0, \hat{x}_2 + y_0\right) \mathrm{d}\theta \mathrm{d}\hat{x}_2.
$$

14

Proof. Let $\mathrm{d}l = \sqrt{1 + \left(\frac{\mathrm{d}\hat{x}_1}{\mathrm{d}\hat{x}_2}\right)^2}\,\mathrm{d}\hat{x}_2$ be the arc measure on the ellipse in Figure 5. Then the surface element on the spheroid of revolution is

$$(4.7) \qquad \mathrm{d}A = \hat{x}_1 \mathrm{d}l \mathrm{d}\theta = \sqrt{p^2 - s^2\hat{x}_2^2 + s^4\hat{x}_2^2}\,\mathrm{d}\theta \mathrm{d}\hat{x}_2.$$

Thus, using equation (4.3) and (4.5) to rewrite $\phi = \hat{\phi} + \phi_0$ in terms of θ, it follows that

$$(4.8)$$
$$R_s f(p, \phi_0, y_0) = \int_{-\frac{p}{s}}^{\frac{p}{s}} \sqrt{p^2 - s^2\hat{x}_2^2 + s^4\hat{x}_2^2} \int_{-\pi}^{\pi} f\left(r, \sin^{-1}\left(\frac{\hat{x}_1}{r}\sin\theta\right) + \phi_0, \hat{x}_2 + y_0\right) \mathrm{d}\theta \mathrm{d}\hat{x}_2,$$

which completes the proof. $\qquad\qquad\qquad\qquad\qquad\qquad\qquad\qquad\qquad\qquad \square$

We now have our main injectivity result.

Theorem 4.3. *For any fixed $s \in (0, 1]$, R_s is injective on domain $L_c^2(C)$, where C is the open unit cylinder .*

Remark 4.4. The following proof uses some similar intuitions to that of [3], applied in that paper to circular Radon transforms. We extend such ideas to three-dimensions, and to spheroid surfaces.

Proof. Let $\epsilon > 0$. We first prove the theorem if $f \in L_c^2(C_\epsilon)$, where

$$(4.9) \qquad C_\epsilon = \left\{\mathbf{x} \in \mathbb{R}^3 : \sqrt{x_1^2 + x_3^2} < 1 - \epsilon\right\}.$$

Let $f \in L_c^2(C_\epsilon)$. Taking the Fourier transform in y_0 on both sides on (4.8) yields

$$\widehat{R_s f}(p, \phi_0, \eta) =$$
$$(4.10)$$
$$2\int_0^{\frac{p}{s}} \cos(\eta\hat{x}_2)\sqrt{p^2 - s^2\hat{x}_2^2 + s^4\hat{x}_2^2} \int_{-\pi}^{\pi} \hat{f}\left(r, \sin^{-1}\left(\frac{\hat{x}_1}{r}\sin\theta\right) + \phi_0, \eta\right) \mathrm{d}\theta \mathrm{d}\hat{x}_2,$$

where η is dual to y_0. We now calculate the Fourier components in ϕ_0 on both sides of (4.10), where $\hat{f}_n(r, \eta) = \frac{1}{2\pi}\int_0^{2\pi} \hat{f}(r, \phi, \eta)e^{-in\phi}\mathrm{d}\phi$:

$$(4.11) \qquad \widehat{R_s f}_n(p, \eta) = 4\int_0^{\frac{p}{s}} \cos(\eta\hat{x}_2)\sqrt{p^2 - s^2\hat{x}_2^2 + s^4\hat{x}_2^2} \int_0^{\pi} \cos(n\hat{\phi})\hat{f}_n(r, \eta)\,\mathrm{d}\theta \mathrm{d}\hat{x}_2.$$

Note that r and $\hat{\phi}$ depend on θ and $\hat{x}_1$ as given in (4.5), with r even as a function of θ, and $\hat{\phi}$ odd as a function of θ.

Making the change of variables $\hat{x}_1 = \sqrt{p^2 - s^2\hat{x}_2^2}$ in the $\hat{x}_2$ integral yields

$$\widehat{R_s f}_n(p, \eta) =$$
$$(4.12)$$
$$\frac{4}{s}\int_0^p \frac{\hat{x}_1\sqrt{\hat{x}_1^2 + s^2(p^2 - \hat{x}_1^2)}}{\sqrt{p^2 - \hat{x}_1^2}} \cos\left(\frac{\eta}{s}\sqrt{p^2 - \hat{x}_1^2}\right) \int_0^{\pi} \cos(n\hat{\phi})\hat{f}_n(r, \eta)\,\mathrm{d}\theta \mathrm{d}\hat{x}_1.$$

Let us now do a change of variables in the θ integral. Using Figure 4 and (4.5), we see $r = \sqrt{\hat{x}_1^2 + 1 - 2\hat{x}_1\cos\theta}$, and $\sin\hat{\phi} = \frac{\hat{x}_1}{r}\sin\theta$. We have

$$\frac{\mathrm{d}r}{\mathrm{d}\theta} = \frac{\hat{x}_1}{r}\sin\theta = \sin\hat{\phi}, \quad \cos\hat{\phi} = \frac{r^2 + 1 - \hat{x}_1^2}{2r}.$$

Then

$$\widehat{R_s f}_n(p, \eta) =$$

(4.13) $\quad \dfrac{4}{s} \displaystyle\int_0^p \dfrac{\hat{x}_1 \sqrt{\hat{x}_1^2 + s^2(p^2 - \hat{x}_1^2)}}{\sqrt{p^2 - \hat{x}_1^2}} \cos\left(\dfrac{\eta}{s}\sqrt{p^2 - \hat{x}_1^2}\right) \int_{1-\hat{x}_1}^{1-\epsilon} \dfrac{T_{|n|}\left(\frac{r^2 + 1 - \hat{x}_1^2}{2r}\right)}{\sqrt{1 - \left(\frac{r^2 + 1 - \hat{x}_1^2}{2r}\right)^2}} \hat{f}_n(r, \eta) \, \mathrm{d}r \mathrm{d}\hat{x}_1$

where $T_{|n|}$ is a Chebyshev polynomial degree $|n|$, $n \in \mathbb{Z}$. Because f is supported in C_ϵ, the upper limit in the inner integral in (4.13) can be $r = 1 - \epsilon$, rather than $r = 1 + \hat{x}_1$. Now, using Fubini's theorem, we see

$$\widehat{R_s f}_n(p, \eta) =$$

(4.14) $\quad \dfrac{4}{s} \displaystyle\int_{1-p}^{1-\epsilon} \int_{1-r}^p \dfrac{\hat{x}_1 \sqrt{\hat{x}_1^2 + s^2(p^2 - \hat{x}_1^2)} \cos\left(\frac{\eta}{s}\sqrt{p^2 - \hat{x}_1^2}\right) T_{|n|}\left(\frac{r^2 + 1 - \hat{x}_1^2}{2r}\right)}{\sqrt{p^2 - \hat{x}_1^2}\sqrt{1 - \left(\frac{r^2 + 1 - \hat{x}_1^2}{2r}\right)^2}} \hat{f}_n(r, \eta) \, \mathrm{d}\hat{x}_1 \mathrm{d}r,$

Substituting $u = 1 - r$ yields

(4.15) $$\widehat{R_s f}_n(p, \eta) = \dfrac{4}{s} \int_0^p K_n(\eta; p, u) \tilde{\hat{f}}_n(u, \eta) \, \mathrm{d}u,$$

a Volterra equation of the first kind, where

(4.16) $\quad K_n(\eta; p, u) = \displaystyle\int_u^p \dfrac{\hat{x}_1 \sqrt{\hat{x}_1^2 + s^2(p^2 - t^2)} \cos\left(\frac{\eta}{s}\sqrt{p^2 - \hat{x}_1^2}\right) T_{|n|}\left(\frac{(1-u)^2 + 1 - \hat{x}_1^2}{2(1-u)}\right)}{\sqrt{p^2 - \hat{x}_1^2}\sqrt{1 - \left(\frac{(1-u)^2 + 1 - \hat{x}_1^2}{2(1-u)}\right)^2}} \mathrm{d}\hat{x}_1,$

and $\tilde{\hat{f}}_n(u, \eta) = \hat{f}_n(1 - u, \eta)$.

To show injectivity, we let $\epsilon_1 \in (0, 1/2)$ and first bound the kernel K_n and its derivative for each fixed η on the set

(4.17) $$D_{\epsilon_1} = \{(p, u) : p \in [\epsilon, 1 - \epsilon_1], \ u \in [\epsilon, p]\}.$$

We have

(4.18)
$$\begin{aligned}
\sqrt{1 - \left(\dfrac{(1-u)^2 + 1 - \hat{x}_1^2}{2(1-u)}\right)^2} &= \sqrt{1 - \left(1 + \dfrac{u^2 - \hat{x}_1^2}{2(1-u)}\right)^2} \\
&= \sqrt{\dfrac{\hat{x}_1^2 - u^2}{1 - u} + \dfrac{(\hat{x}_1^2 - u^2)(u^2 - \hat{x}_1^2)}{4(1-u)^2}} \\
&= \dfrac{\sqrt{\hat{x}_1^2 - u^2}}{\sqrt{1 - u}} \sqrt{1 + \dfrac{u^2 - \hat{x}_1^2}{4(1-u)}}.
\end{aligned}$$

16

Thus
(4.19)

$$K_n(\eta; p, u) = \sqrt{1-u} \int_u^p \frac{\hat{x}_1 \sqrt{\hat{x}_1^2 + s^2(p^2 - \hat{x}_1^2)} \cos\left(\frac{\eta}{s}\sqrt{p^2 - \hat{x}_1^2}\right) T_{|n|}\left(\frac{(1-u)^2 + 1 - \hat{x}_1^2}{2(1-u)}\right)}{\sqrt{p^2 - \hat{x}_1^2}\sqrt{\hat{x}_1^2 - u^2}\sqrt{1 + \frac{u^2 - \hat{x}_1^2}{4(1-u)}}} d\hat{x}_1$$

$$= \sqrt{1-u} \int_0^1 \frac{\hat{x}_1 \sqrt{\hat{x}_1^2 + s^2(p^2 - \hat{x}_1^2)} \cos\left(\frac{\eta}{s}\sqrt{p^2 - \hat{x}_1^2}\right) T_{|n|}\left(\frac{(1-u)^2 + 1 - \hat{x}_1^2}{2(1-u)}\right)}{\sqrt{v}\sqrt{1-v}\sqrt{p + \hat{x}_1}\sqrt{\hat{x}_1 + u}\sqrt{1 + \frac{u^2 - \hat{x}_1^2}{4(1-u)}}} \Big|_{\hat{x}_1 = u + v(p-u)} dv,$$

after substituting

(4.20)
$$\hat{x}_1 = u + v(p - u)$$

in the last step. We have

$$K_n(\eta; p, p) = \frac{p\sqrt{1-p}}{2} \int_0^1 \frac{1}{\sqrt{v}\sqrt{1-v}} dv$$

(4.21)
$$= \frac{\pi p \sqrt{1-p}}{2},$$

and thus $K_n(\eta, \cdot, \cdot)$ is non-zero on the diagonal, unless $p = 0, 1$, for all $\eta \in \mathbb{R}$ and $n \in \mathbb{Z}$. The support of f is bounded away from the cylinder surface and we are considering $p \in [\epsilon, 1 - \epsilon_1]$, and thus we do not consider $p = 0, 1$.

We will now show that $K_n(\eta; p, u)$ and $\frac{d}{dp} K_n(\eta; p, u)$ are bounded for each η and all $(p, u) \in D_{\epsilon_1}$. To do this, we show that all the terms dependent on p under the integral on the second line of (4.19) are bounded and have bounded first order derivative with respect to p. First we have $|\hat{x}_1| \le 1$ and from the change of variable (4.20), $\frac{d}{dp}\hat{x}_1 = v \le 1$. Now

$$\sqrt{\hat{x}_1^2 + s^2(p^2 - \hat{x}_1^2)} = \sqrt{(1 - s^2)\hat{x}_1^2 + s^2 p^2} \le \sqrt{(1 - s^2) + s^2} = 1,$$

and

$$\frac{d}{dp}\sqrt{(1 - s^2)\hat{x}_1^2 + s^2 p^2} = \frac{ps^2 + v(1 - s^2)\hat{x}_1}{\sqrt{(1 - s^2)\hat{x}_1^2 + s^2 p^2}} \le \frac{1}{\sqrt{(1 - s^2)\epsilon^2 + s^2\epsilon^2}} = \frac{1}{\epsilon},$$

noting $\hat{x}_1 \ge u \ge \epsilon$ and $p > \epsilon$. We have $\left|\cos\left(\frac{\eta}{s}\sqrt{p^2 - \hat{x}_1^2}\right)\right| \le 1$, and

$$\frac{d}{dp}\cos\left(\frac{\eta}{s}\sqrt{p^2 - \hat{x}_1^2}\right) = -\frac{\frac{\eta}{s}(p - v\hat{x}_1)}{\sqrt{p^2 - \hat{x}_1^2}}\sin\left(\frac{\eta}{s}\sqrt{p^2 - \hat{x}_1^2}\right)$$

(4.22)
$$= -\left(\frac{\eta}{s}\right)^2 (p - v\hat{x}_1) \operatorname{sinc}\left(\frac{\eta}{s}\sqrt{p^2 - \hat{x}_1^2}\right),$$

and thus $\left|\frac{d}{dp}\cos\left(\frac{\eta}{s}\sqrt{p^2 - \hat{x}_1^2}\right)\right| \le \left(\frac{\eta}{s}\right)^2$. For $n \ne 0$, we have $\left|T_{|n|}\left(\frac{(1-u)^2 + 1 - \hat{x}_1^2}{2(1-u)}\right)\right| \le 1$ and

$$\frac{d}{dp}T_{|n|}\left(\frac{(1-u)^2 + 1 - \hat{x}_1^2}{2(1-u)}\right) = -\frac{v\hat{x}_1}{1-u}T'_{|n|}\left(\frac{(1-u)^2 + 1 - \hat{x}_1^2}{2(1-u)}\right)$$

(4.23)
$$= -\frac{|n|v\hat{x}_1}{1-u}U_{|n|-1}\left(\frac{(1-u)^2 + 1 - \hat{x}_1^2}{2(1-u)}\right),$$

17

where U_n is a Chebyshev polynomial of the second kind. It follows that

$$\left| \frac{d}{dp} T_{|n|} \left(\frac{(1-u)^2 + 1 - \hat{x}_1^2}{2(1-u)} \right) \right| \leq \frac{|n|^2}{\epsilon_1},$$

using Figure 4 and the Law of Cosines, that $|U_{|n|}(x)| \leq |n| + 1$ for $|x| \leq 1$, and $\frac{1}{1-u} \leq \frac{1}{\epsilon_1}$. The $n = 0$ case is trivial since $T_0 = 1$.

Now, we have $\frac{1}{\sqrt{p+\hat{x}_1}\sqrt{\hat{x}_1+u}} \leq \frac{1}{2\epsilon}$ and

$$\frac{d}{dp} \left(\frac{1}{\sqrt{p+\hat{x}_1}\sqrt{\hat{x}_1+u}} \right) = \frac{1+2v}{\sqrt{p+\hat{x}_1}\sqrt{\hat{x}_1+u}} \leq \frac{3}{2\epsilon}.$$

Finally, we have

$$\frac{u^2 - \hat{x}_1^2}{4(1-u)} \geq \frac{u^2 - 1}{4(1-u)} = -\frac{(u+1)}{4} \geq -\frac{1}{2}.$$

Thus, $\left(1 + \frac{u^2-\hat{x}_1^2}{4(1-u)} \right)^{-\frac{1}{2}} \leq \sqrt{2}$, and

$$\frac{d}{dp} \left(1 + \frac{u^2 - \hat{x}_1^2}{4(1-u)} \right)^{-\frac{1}{2}} = \frac{v\hat{x}_1}{4(1-u)} \left(1 + \frac{u^2 - \hat{x}_1^2}{4(1-u)} \right)^{-\frac{3}{2}} \leq \frac{1}{\epsilon_1\sqrt{2}}.$$

After putting all this together, we can convert (4.15) into a Volterra equation of the second kind with bounded kernel for $(p, u) \in D_{\epsilon_1}$ and invert by successive approximations using classical Volterra Integral equation theory [35, 30]. Therefore, if $R_s f = 0$, then (4.15) implies that $\hat{f}_n(r, \eta) = 0$ for all η and for $r \in [\epsilon_1, 1 - \epsilon]$. The lower limit of ϵ_1 was used only to show K_n is bounded and so $\hat{f}_n(r, \eta) = 0$ for all $r \in [0, 1 - \epsilon]$.

Thus, any $f \in L_c^2(C)$ is uniquely determined by $R_s f$, for any fixed $s \in (0, 1]$. This implies that R_s is injective on $L_c^2(C)$. $\qquad\square$

Remark 4.5. Note that the proof requires f to be zero near the boundary of the cylinder. This is needed so that the inner integral in (4.13) can have upper limit $1 - \epsilon$ instead of 1. This allows us to prove that K satisfies the hypotheses to make (4.15) an invertible Volterra equation.

The standard inversion result for Volterra equations would not apply to K_n if that upper limit were 1 since K_n would no longer be bounded. This suggests there could be a null space for R_s on $L^2(C)$.

We now discuss the visible singularities.

4.2. **Visible singularities.** In this section, we investigate the singularity coverage (or edge detection) using spheroid and spherical integral data when the surface of sources and receivers is a unit cylinder with central axis x_2, as considered in the previous section on injectivity. Let ∂C denote the cylinder of source and receiver positions. We consider ϕ and x_2 in the range $\phi \in [0, 2\pi]$ and $x_2 \in [-1, 1]$, and parameterize ∂C using cylindrical coordinates $\mathbf{s}(\phi, x_2) = (\cos\phi, x_2, \sin\phi) \in \partial C$, as in (4.1) For every $\mathbf{x} \in \{\sqrt{x_1^2 + x_3^2} < 1\} = C_I$ (i.e., for every $\mathbf{x}$ in the interior of ∂C), we can calculate the proportion of wavefront directions that are detected by spherical and spheroid integral data. The spherical data is three-dimensional, and the degrees of freedom are (p, ϕ_0, y_0). The spheroid data is four-dimensional, with degrees of freedom (s, p, ϕ_0, y_0). We wish to investigate whether the additional scaling factor, s, offers any improvement in terms of edge detection. We discretize ∂C with ϕ at $1°$ intervals,

$\phi \in \{\frac{j\pi}{180} : 0 \le j \le 179\} = \Phi$, and $x_2 \in \{-1 + \frac{2j}{N-1} : 0 \le j \le N - 1\} = X_2$, where $N \ge 1$ controls the level of discretization along the x_2 axis. For the spherical data, we consider all spheres with centers $c \in \{(\cos\phi, x_2, \sin\phi) : \phi \in \Phi, x_2 \in X_2\} = \partial C_0$. We consider all spheroids with axis of revolution parallel to x_2, whose foci $c_1, c_2 \in \partial C_0$. For every given c and $\mathbf{x} \in C_I$, we calculate the wavefront direction, $\xi = \frac{\mathbf{x}-c}{\|\mathbf{x}-c\|}$, detected. For every $\mathbf{x} \in C_I$, we calculate all $180 \times N$ wavefront directions detected at $\mathbf{x}$, and use this information to build a 3-D map of the total wavefront detection on C_I. Similarly, we can calculate a 3-D map of the directional coverage for the spheroid integral data, and compare against the spherical map.

4D spheroid data   3D sphere data   3D sphere data - cropped color bar
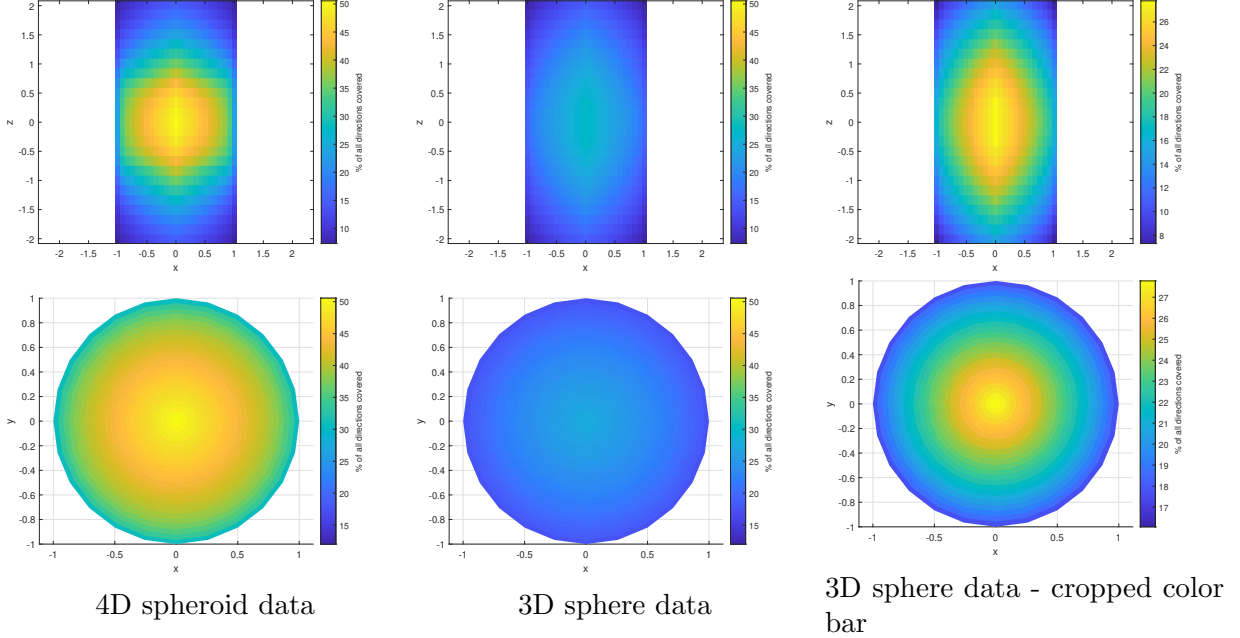
FIGURE 6. Detectable singularities when $N = 50$. Top row - (x_1, x_2) plane. Bottom row - (x_1, x_3) plane. Left - 4D spheroid data. Middle - 3D sphere data. Right - 3D sphere data with cropped color bar to better show the details.

In Figure 6, we present (x_1, x_3) and (x_1, x_2) plane cross-sections showing the directional coverage using spherical and spheroid data when $N = 50$. The left-hand and middle columns of Figure 6 compare the directional coverage of spheroid and spherical data on the same scale. The right-hand column of Figure 6 shows the spherical wavefront detection with the color bar cropped so that the reader can better see the details. We can see that the wavefront coverage is significantly stronger using spheroid integral data, when compared to spherical, and thus the additional degree of freedom, s, has proven beneficial.

To show what happens as the number of emitters, and level of x_2 discretization (N), varies, we plot curves of the average directional coverage over the (x_2, x_3) and (x_1, x_3) planes for varying N in Figure 7. For all $N \le 100$, spheroid data offers greater average wavefront detection, when compared to spherical, for all $N \le 100$, although the difference becomes less pronounced with increasing N.

Let $R_E(s, p, \phi_0, y_0) = R_s(p, \phi_0, y_0)$. If one were to design a URT scanner with a cylindrical set of emitters/receivers, as described in this section, it would be beneficial to measure
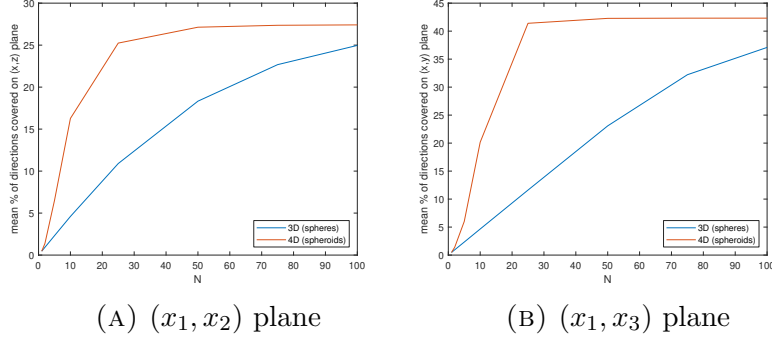
(A) (x_1, x_2) plane   (B) (x_1, x_3) plane

FIGURE 7. Mean directional coverage percentage over (x_1, x_2) and (x_1, x_3) plane cylinder cross-sections for varying N.

spheroid integral data, $R_E f$, over $R_1 f$ (spherical) data, as R_E offers greater edge detection, especially with more limited emitter/receiver discretization. R_E and R_1 both have the theoretical guarantees of injectivity and satisfaction of Bolker, as proven by our microlocal and injectivity theorems.

5. EXAMPLE IMAGE RECONSTRUCTIONS IN TWO-DIMENSIONS

In this section, we present two-dimensional image reconstructions from spherical (circular) integral data. We consider two scanning curves, S, one which is non-convex, and one which is convex. We verify Corollary 3.2 by comparing the artifacts in (unfiltered) backprojection reconstructions of delta functions to artifacts predicted by our theory. In addition, we also investigate techniques to suppress the image artifacts in the non-convex curves case. Specifically, we apply discrete solvers and a Total Variation (TV) regularizer with smoothing parameter chosen by cross validation.

We define the Radon transform

$$(5.1) \qquad R_c f(r, y_1) = Rf\left((y_1, q(y_1))^T, I_{2\times2}, r^2\right),$$

where q defines the set of circle centers, $S = q(\mathbb{R})$, and r is the circle radius. In this section, we present reconstructions of f from $R_c f$ data. We consider two example q, one non-convex with $q(y_1) = a(y_1 + 100)(y_1 - 100)y_1^2 + 100$ and $a = 5/10^6$, and one convex, with $q(y_1) = \frac{x^2}{50} - 100$. See Figure 8 for an illustration of both curves. In both cases, $\text{supp}(f) \subset \{(x_1, x_2) \in \mathbb{R}^2 : x_2 > q(x_1), |x_1| < 100\}$. These example curves and function supports are chosen for two reasons. First, for $f \in L_c^2(D)$, $R_c f$ uniquely determines f for both q considered, and hence there are no artifacts due to a null space. This is true since S, for both q in Figure 8, is not the union of a finite set and a Coxeter system of straight lines [1]. Second, $R_c f$ detects all singularities in D. Thus, the only artifacts are due to noise and the Bolker condition, which is our focus. We will also discover later, due to discretization limitations, streaking artifacts which occur along circles at the boundary of the data set. Similar boundary artifacts have been discussed previously in the literature, in regards to photo-acoustic tomography and sonar [13].

5.1. **Delta function reconstructions.** We now present unfiltered backprojection image reconstructions of delta functions to validate the results of Theorem 3.1. A delta function
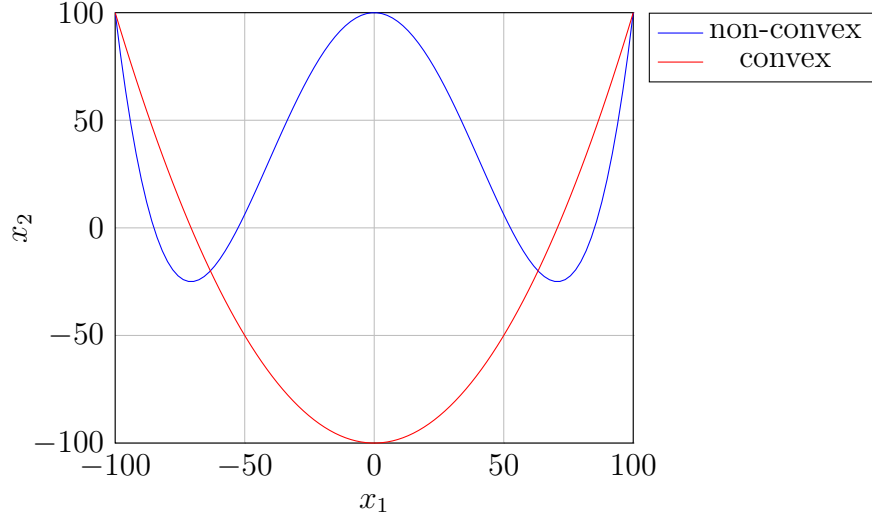
FIGURE 8. Convex and non-convex measurement curve examples.

predicted artifacts $A^T A\delta$ (observed artifacts)
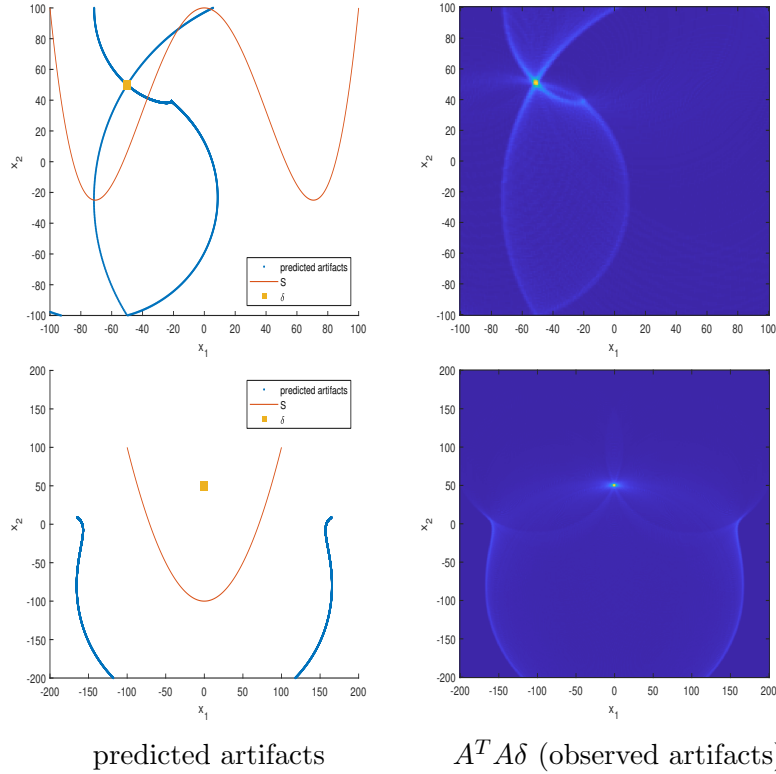
FIGURE 9. Predicted observed artifacts in delta function reconstructions. Top row - non-convex curve. Bottom row - convex curve.

is supported at a single point and has singularities (edges) in all directions. Thus, in a reconstruction of a delta function, δ, from circular integral data with centers on $S = q(\mathbb{R})$, we would expect to see artifacts which are the reflections of δ in planes tangent to S. Let A denote the discretized form of R_c. We sample circle centers $c_i = \left(-100 + \frac{i-1}{2}, q\left(-100 + \frac{i-1}{2}\right)\right)$

21

for $0 \leq i \leq 401$, and radii $r_j = 1 + j$ for $1 \leq j \leq 199$. See the right column of Figure 9 for example backprojection reconstructions of delta functions when S is convex and non-convex. In the left column of Figure 9, we show the artifacts due to Bolker as predicted by our theory. The predicted and observed artifacts match up well, and all artifact locations in the convex case lie outside the function support, which is in line with Theorem 3.1. In the bottom-right of Figure 9, there are additional circular shaped streaking artifacts which pass through the delta function. The circular streaks have centers at the end points of the red curve in the bottom-left of Figure 9. These occur due to the sharp cutoff at the boundary of the sinogram, since the circle centers are only finitely sampled. The boundary artifacts are less noticeable in the non-convex curve case, in the top-right of Figure 9, and the artifacts due to Bolker appear more strongly.

5.2. **Phantom reconstructions.** Here, we present algebraic reconstructions of image phantoms from circular integral data. We consider two phantoms, one simple and one complex. The simple phantom consists of two rectangles with density 1, and the complex phantom is made up of a thin cross, a square, a hollow ellipse, and two circular phantoms, all of varying densities. The nonzero densities are arranged to fit within D, for both the convex and non-convex measurement curves considered. We present reconstructions using the Landweber method and TV regularization. Specifically, to implement TV, we find

$$(5.2) \qquad \arg\min_{\mathbf{x}} (A\mathbf{x} - \mathbf{b})^T (A\mathbf{x} - \mathbf{b}) + \alpha\sqrt{\|\nabla\mathbf{x}\|_2^2 + \beta^2},$$
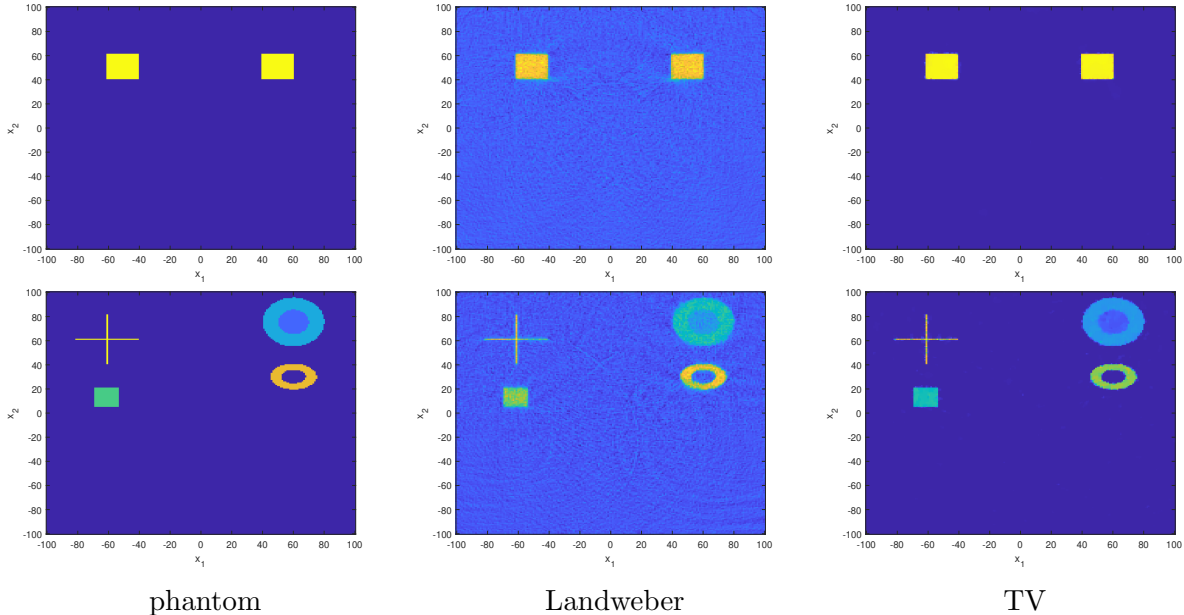
where $\alpha, \beta > 0$ are regularization parameters.

FIGURE 10. Reconstructions of image phantoms - non-convex curve.

The data was simulated by $\mathbf{b} = A_\epsilon \mathbf{x} + \eta$, where A_ϵ is a perturbed A. Specifically, to generate A_ϵ, the non-zero values of A (i.e., the circular integral weights) were multiplied by $1 + u$, where $u \sim U(-0.5, 0.5)$, that is, u is drawn from a uniform distribution on $[-0.5, 0.5]$.

We use A_ϵ to generate data to avoid inverse crime. The added noise is white noise drawn from a standard Gaussian $\eta \sim \mathcal{N}(0, \sigma)$, where σ controls the noise level. The hyperparameters α, β were chosen using cross-validation, so there is no optimism in the results with respect to the selection of α, β.
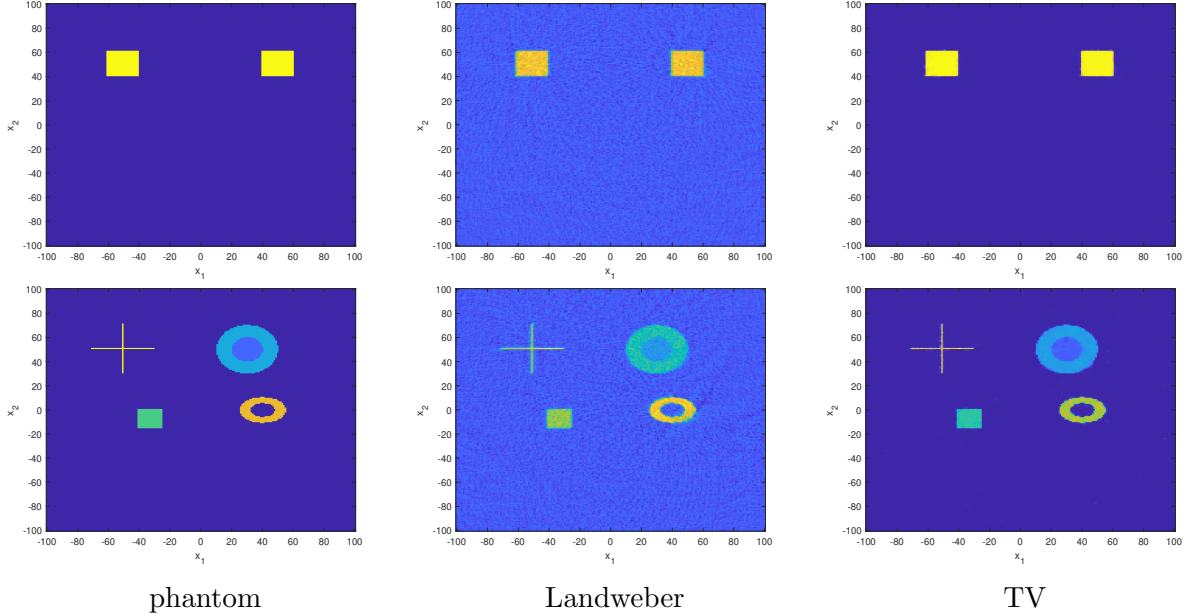

phantom   Landweber   TV

FIGURE 11. Reconstructions of image phantoms - convex curve.

See Figure 10, where we show reconstructions of the test phantoms using the Landweber method and TV in the non-convex curve case. We see severe artifacts in the Landweber reconstructions, which is not surprising given the inversion instabilities of R when S does not satisfy global convexity. The artifacts are largely suppressed in the TV reconstructions. TV enforces sparse gradients, and thus it TV can combat additional, unwanted singularities in the reconstruction due to Bolker. In this example, TV is effective in removing the artifacts.

In Figure 11, we present image reconstruction of the simple and complex phantom in the convex curve case. The artifacts in the Landweber reconstruction of the simple phantom are minimal and we see only a background noise effect. In the Landweber reconstruction of the complex phantom, there are mild artifacts which appear as a streaking effect near the boundary of the hollow ellipse. In the TV reconstructions of both phantoms, the noise effects and streaking artifacts are suppressed.

6. Conclusions and further work

In this paper, we presented novel microlocal and injectivity results for a new generalized Radon transform, R, which defines the integrals of square integrable compactly supported functions over ellipsoids, hyperboloids, and elliptic hyperboloids and generalizations with centers on a smooth surface, S. We showed that R was an FIO and proved that R satisfied the Bolker condition if condition (3.3) holds, and this is if and only if when M is dimension zero. We applied our theory to some examples in section 3.2, and provided a more in-depth analysis of a cylindrical scanning geometry of interest in URT, where we proved injectivity

results. Specifically, we showed that any $f \in L_c^2$, with support in a cylindrical tube, could be reconstructed uniquely from its integrals over spheroids with centers on a cylinder which encloses the support of f. We also investigated the visible singularities for the cylindrical geometry in section 4.2. In section 5, to validate our microlocal theory and show the image artifacts, we presented image reconstructions of delta functions and image phantoms. We also tested a method of artifact reduction, using TV regularization and cross-validation, which proved successful in the simulations conducted.

In further work, we aim to investigate the potential practical applicability of the hyperboloid and elliptic hyperboloid Radon transform, as, in this work, we considered only applications of R in fields such as URT, where the integral surfaces are spheroids. There is indication that the hyperboloid case may be of interest in proton therapy through the measurement of multiple gamma rays emitted as a cascade [28]. We aim also to pursue three-dimensional image reconstruction methods for the cylindrical scanning geometry introduced in section 3.2. As evidenced in section 4.2, the inverse of R in the cylindrical case is severely unstable, as there are invisible singularities. Thus, it is likely that we will require strong regularization (e.g., TV or machine learning) to solve this problem.

References

[1] M. L. Agranovsky and E. T. Quinto. Injectivity sets for the Radon transform over circles and complete systems of radial functions. *Journal of Functional Analysis*, 139(2):383–414, 1996.

[2] G. Ambartsoumian, J. Boman, V. P. Krishnan, and E. T. Quinto. Microlocal analysis of an ultrasound transform with circular source and receiver trajectories. In *Geometric analysis and integral geometry*, volume 598 of *Contemp. Math.*, pages 45–58. Amer. Math. Soc., Providence, RI, 2013.

[3] G. Ambartsoumian, R. Gouia-Zarrad, and M. A. Lewis. Inversion of the circular radon transform on an annulus. *Inverse Problems*, 26(10):105015, 2010.

[4] L.-E. Andersson. On the determination of a function from spherical averages. *SIAM Journal on Mathematical Analysis*, 19(1):214–232, 1988.

[5] P. Caday. Cancellation of singularities for synthetic aperture radar. *Inverse Problems*, 31(1):015002, 22, 2015.

[6] J. D. Coker and A. H. Tewfik. Multistatic sar image reconstruction based on an elliptical-geometry radon transform. In *2007 International Waveform Diversity and Design Conference*, pages 204–208. IEEE, 2007.

[7] A. M. Cormack. Representation of a function by its line integrals with some radiological applications. *J. Appl. Physics*, 34(9):2722–2727, 1963.

[8] J. J. Duistermaat. *Fourier integral operators*, volume 130 of *Progress in Mathematics*. Birkhäuser, Inc., Boston, MA, 1996.

[9] J. J. Duistermaat and L. Hormander. *Fourier integral operators*, volume 2. Springer, 1996.

[10] R. Felea. Displacement of artefacts in inverse scattering. *Inverse Problems*, 23(4):1519–1531, 2007.

[11] R. Felea, R. Gaburro, and C. J. Nolan. Microlocal analysis of sar imaging of a dynamic reflectivity function. *SIAM Journal on Mathematical Analysis*, 45(5):2767–2789, 2013.

[12] R. Felea, V. P. Krishnan, C. J. Nolan, and E. T. Quinto. Common midpoint versus common offset acquisition geometry in seismic imaging. *Inverse Probl. Imaging*, 10(1):87–102, 2016.

[13] J. Frikel and E. T. Quinto. Artifacts in incomplete data tomography with applications to photoacoustic tomography and sonar. *SIAM J. Appl. Math.*, 75(2):703–725, 2015.

[14] R. Gouia-Zarrad and G. Ambartsoumian. Approximate inversion algorithm of the elliptical radon transform. In *2012 8th International Symposium on Mechatronics and its Applications*, pages 1–4. IEEE, 2012.

[15] C. Grathwohl, P. C. Kunstmann, E. T. Quinto, and A. Rieder. Imaging with the elliptic radon transform in three dimensions from an analytical and numerical perspective. *SIAM Journal on Imaging Sciences*, 13(4):2250–2280, 2020.

[16] V. Guillemin and S. Sternberg. *Geometric Asymptotics*. American Mathematical Society, Providence, RI, 1977.

[17] M. Haltmeier and S. Moon. The spherical radon transform with centers on cylindrical surfaces. *Journal of Mathematical Analysis and Applications*, 448(1):567–579, 2017.

[18] A. Homan and H. Zhou. Injectivity and Stability for a Generic Class of Generalized Radon Transforms. *J Geom Anal*, 27:1515–1529, 2017.

[19] L. Hörmander. *The analysis of linear partial differential operators. I.* Classics in Mathematics. Springer-Verlag, Berlin, 2003. Distribution theory and Fourier analysis, Reprint of the second (1990) edition [Springer, Berlin].

[20] L. Hörmander. *The analysis of linear partial differential operators. III.* Classics in Mathematics. Springer, Berlin, 2007. Pseudo-differential operators, Reprint of the 1994 edition.

[21] L. Hörmander. *The analysis of linear partial differential operators. IV.* Classics in Mathematics. Springer-Verlag, Berlin, 2009. Fourier integral operators, Reprint of the 1994 edition.

[22] J. Klein. Inverting the spherical radon transform for physically meaningful functions. *arXiv preprint math/0307348*, 2003.

[23] V. P. Krishnan, H. Levinson, and E. T. Quinto. Microlocal analysis of elliptical radon transforms with foci on a line. In *The mathematical legacy of Leon Ehrenpreis*, pages 163–182. Springer, 2012.

[24] L. A. Kunyansky. Explicit inversion formulae for the spherical mean radon transform. *Inverse problems*, 23(1):373, 2007.

[25] S. Moon and J. Heo. Inversion of the elliptical radon transform arising in migration imaging using the regular radon transform. *Journal of Mathematical Analysis and Applications*, 436(1):138–148, 2016.

[26] L. V. Nguyen and T. A. Pham. Microlocal analysis for spherical Radon transform: two nonstandard problems. *Inverse Problems*, 35(7):074001, 15, 2019.

[27] V. P. Palamodov. A uniform reconstruction formula in integral geometry. *Inverse Problems*, 28(6):065014, 2012.

[28] C. M. Panaino, R. I. Mackay, M. Sotiropoulos, K. J. Kirkby, and M. J. Taylor. Full 3d position reconstruction of a radioactive source based on a novel hyperbolic geometrical algorithm. *Computer Physics Communications*, 252, 2020.

[29] E. T. Quinto. The dependence of the generalized Radon transform on defining measures. *Trans. Amer. Math. Soc.*, 257:331–346, 1980.

[30] E. T. Quinto. The invertibility of rotation invariant Radon transforms. *J. Math. Anal. Appl.*, 94:602–603, 1983.

[31] B. Rubin. Inversion formulas for the spherical radon transform and the generalized cosine transform. *Advances in Applied Mathematics*, 29(3):471–497, 2002.

[32] B. Rubin. A note on the sonar transform and related Radon transforms. *arXiv:2206.05854 [math.FA]*, page 13, 2022.

[33] W. Rudin. *Functional analysis*. McGraw-Hill Book Co., New York, 1973. McGraw-Hill Series in Higher Mathematics.

[34] P. Stefanov and G. Uhlmann. Is a curved flight path in SAR better than a straight one? *SIAM J. Appl. Math.*, 73(4):1596–1612, 2013.

[35] F. G. Tricomi. *Integral equations*. Dover Publications, Inc., New York, 1985. Reprint of the 1957 original.

[36] J. W. Webber and S. Holman. Microlocal analysis of a spindle transform. *Inverse Problems & Imaging*, 13(2):231–261, 2019.

[37] J. W. Webber and E. T. Quinto. Microlocal analysis of a compton tomography problem. *SIAM Journal on Imaging Sciences*, 13(2):746–774, 2020.